Microroughness-induced disturbances in supersonic blunt body flow

Thomas Schilden,[1,*] Alexej Pogorelov,[1] Sohel Herff,[1] and Wolfgang Schröder[1,2]
[1]Chair of Fluid Mechanics and Institute of Aerodynamics, RWTH Aachen University, 52062 Aachen, Germany
[2]JARA Center for Simulation and Data Science, RWTH Aachen University, 52074 Aachen, Germany

(Received 13 September 2019; accepted 30 April 2020; published 26 June 2020)

To identify the mechanism triggering boundary layer transition on a spherical forebody of an Apollo type re-entry capsule direct numerical simulations of perturbed flow are analyzed. The perturbations are generated by deterministic distributed surface roughnesses that resemble model surface imperfections that are mounted on a capsule model and are experimentally investigated in Radespiel *et al.* [J. Spacecr. Rockets **56**, 405 (2019)]. Therein, the role of distributed roughness in the transition scenario was highlighted but the mechanism remained unclear. In this manuscript, the sensitivity of the flow perturbations with respect to the roughness layout is investigated. The great span of spatial scales, i.e., capsule diameter, boundary layer thickness, and micro-size roughness, define the requirements of the numerical method. Modifications to a finite-volume unstructured Cartesian cut-cell method to meet these requirements are presented. The receptivity of the capsule boundary layer to the roughness and the subsequent disturbance growth are analyzed. The roughness properties at the most downstream position govern the flow perturbation. The impact of the streamwise character of the roughness layout is intensified by increasing the Reynolds number of the flow. The growth mechanism is identified as transient growth and the most amplified disturbances are compared to the results of optimal transient growth theory. Streamwise vortices cause growth via the lift-up effect. However, the wall normal scales of optimal and roughness induced disturbance differ significantly leading to suboptimal growth.

DOI: 10.1103/PhysRevFluids.5.063903

I. INTRODUCTION

The state of a boundary layer covering a solid body, which can be laminar, transitional, or turbulent, highly influences the balance of momentum and energy between body and fluid. As a direct consequence, propulsion, gravity, or loss of momentum balance the body forces and thermal loads need to be sustained. The latter problem is a major aero- and aerothermodynamic design parameter for vehicles in supersonic flows [1–4].

Re-entry vehicles pose a prominent case for the aforementioned problem. On the one hand, re-entry capsules are designed to ensure safe operation, i.e., undamaged atmospheric re-entry of equipment and/or crew. On the other hand, the thermal loads require a thermal protection system (TPS) reducing the payload of rockets [5]. Therefore, the TPS is a delicate subject in the design process of re-entry capsules.

In the first half of the Apollo program during the early 1960s, the smooth part of the TPS was successfully designed using laminar stagnation point flow heating prediction methods based on, e.g., Lees [6] or Fay and Riddle [7], wind tunnel tests, and a supporting flight program [8–10]. The final design was considered conservative due to technological uncertainties [11]. Nowadays, the

*t.schilden@aia.rwth-aachen.de

philosophy for the development of the Orion Crew Exploration Vehicle (CEV) is to rely primarily on computational methods [12]. The uncertainties of the computational methods covering various subjects were assessed by corresponding experiments [12–15]. To evaluate the prediction of the convective heating rate of the TPS wind tunnel experiments were compared to Navier-Stokes simulations of laminar and turbulent flow based on the Reynolds-averaged Navier-Stokes (RANS) equations [14,15]. Even for nominally smooth capsules, transitional or fully turbulent flow on the leeward capsule forebody was found in the experiments. The unknown transition mechanism constitutes a severe uncertainty in the heating rate prediction and thus, contributes to the policy of assuming fully turbulent flow throughout the re-entry trajectory [12,15]. This precondition leads to a TPS which is locally overengineered for peak heating rates and entirely oversized for the integrated heat load. Therefore, to develop an advanced TPS design with reduced weight satisfying aerospace safety regulations, laminar-turbulent transition has to be predicted [5,10,12].

Reliable predictions are preferably based on the understanding of the physical mechanisms rather than just data and therefore, boundary layer stability theory was considered [16,17]. Whereas sphere-cone shaped forebodies permit modal growth of boundary layer instabilities, capsules with spherical forebodies still raise questions considering the dominant mechanism of transition [18,19]. The accelerated cooled boundary layer should stabilize the laminar flow and cross flow was known to be weak for capsules at considerable angle of attack [20–22]. At any rate, transition occurs and therefore, the mechanisms of transition on re-entry capsules are still under investigation [23,24]. In the following, the state of the art in this research area is briefly discussed.

Extensive numerical investigations based on simulations of the steady Navier-Stokes equations and various stability analyses featuring corresponding experimental results clarified the process of how transition on the spherical forebody of an Apollo type capsule is initiated [25–27]. First, modal instabilities and transition at 24° angle of attack were investigated in Ref. [26]. The pressure gradient on the forebody is entirely favorable and whether normal or oblique instability due to first modes were numerically determined in the operating range of the experimental facility. Furthermore, very low cross flow velocities occurred and a stability analysis did not reveal any amplified steady or traveling cross-flow modes for wind tunnel conditions. The experimental results showed transitional flow near the leeward shoulder of the capsule using a temperature sensitive paint coating causing a mean arithmetic roughness height $R_a = 10\ \mu$m. The findings of a highly polished capsule were in very good agreement with the numerically determined laminar flow. In a second step, the apparent importance of surface roughness was investigated by modal stability analyses of single roughness elements on the capsule forebody using two- and three-dimensional stability theory complemented by experimental data [25,27]. The height of the roughness elements was in the range between 75 to 150 μm resulting in a roughness Reynolds number Re_{kk}, i.e., the Reynolds number based on the roughness height and the unperturbed flow at that height, of 124 to 336. Modal growth occurs in the wake closely downstream of the elements but the streamwise extent of the amplified region is small due to the overall favorable pressure gradient. Traces of the instability modes were also found in the experiments. However, although modal instability downstream of single roughness elements can trigger transition on the Apollo type capsule, this is not the type of transition documented in Ref. [26]. That is, the $R_a = 10\ \mu$m roughness was distributed and Re_{kk} was an order of magnitude lower than for the single roughness. Therefore, it is conjectured that micro-size distributed roughness initiates transition and the subsequent mechanism of amplification is nonmodal transient growth. This growth mechanism is associated with the nonorthogonal operator of the linearized disturbance equations [28].

This conclusion agrees with the findings of the blunt body paradox, i.e., early transition on spherical forebodies in supersonic flows [18,29–33]. A review on transient growth in the context of blunt body flow and a numerical investigation of possible transient growth on the windward side of a sphere is given in Ref. [34]. Corresponding capsules are investigated numerically in Ref. [23]. Optimal boundary layer disturbance growth was found for steady streamwise vortices that subsequently turn into streamwise velocity streaks. This mechanism is denoted lift-up effect [35].

However, roughness induced transient growth, whose flow field is defined by streamwise vortices in a streamwise velocity wake, is possible but always suboptimal [34].

The link between roughness, transient growth, and transition was earlier proposed by Reshotko and Tumin [30,32]. In Ref. [30], disturbance amplification in stagnation point flows by transient growth was shown to be a candidate to lead to transition. Roughness was suspected to generate the initial disturbance. The investigation in Ref. [32] led to a correlation based on theory and observation. The correlation incorporates receptivity of the boundary layer to roughness as the initial disturbance, the successive transient growth is based on numerical data, and a threshold for transition that has been retrieved from experimental results. The validity of this new correlation to transition data by Reda [36,37] and the passive nosetip technology (PANT) program [38] is remarkable. The height of the roughness divided by the momentum thickness of the laminar boundary layer k/Θ enters the correlation. The k/Θ data from Refs. [36–38] agree with the correlation in Ref. [32] approximately in the range of 0.5 to 7. Smaller roughness was also investigated experimentally in the PANT program but the data showed different behavior and were excluded [38]. The dominant mechanism for transition in that case was suspected to be triggered by freestream disturbances. Also the recent experiments in Refs. [24,39] corroborate the finding of Reshotko and Tumin, i.e., the correlation predicts the measurements. For the transitional data in Ref. [26], k/Θ is <0.5 and below the range of data to agree with the transient growth based correlation by Reshotko and Tumin. Similarly to the aforementioned excluded PANT data, freestream disturbances can be suspected to become an additional factor.

An inventive experimental study supporting the influence of freestream disturbances was conducted in Ref. [40]. The PANT transition data could be extended to lower ratios of roughness height and momentum thickness k/Θ using nozzle throat boundary layer transition data. With decreasing roughness height, transition to turbulence becomes independent of the roughness and is attributed to the facility, e.g., freestream disturbances. To clarify the transition scenario for the distributed surface imperfection of $R_a = 10$ μm observed in Ref. [26], distributed deterministic micro-size roughness on a blunt body under varying freestream disturbance conditions was experimentally investigated in Ref. [24].

Compared to the flow in Ref. [26], the deterministic surface imperfections in Ref. [24] are well defined and allow equivalent numerical simulations. The experiments of Ref. [24] are summarized in Fig. 1. The Schlieren image shows the Apollo type re-entry capsule at 24° angle of attack. The flow is from left to right and the dark region in the flow upstream of the capsule is created by the shock wave. From the stagnation point "sp" over the leeward side of the capsule forebody, i.e., toward the body fitted η^* scale, the boundary layer is accelerated. The distributed roughness is placed at $\eta^* = 0$ and heat flux measurements in the range $0 < \eta^* < 1$ are utilized to investigate boundary layer transition. Figure 1(b) shows the surface heat flux of four flow configurations that motivated the present investigation. Placing a clean capsule model in the reference position off the wind tunnel centerline—denoted by "clean & ref pos"—constitutes the laminar reference flow. Neither adding surface imperfections labeled "rough & ref pos" nor increasing the freestream disturbances visualized by the "clean & in wake" distribution leads to a substantial heat flux increase. Note that in this wind tunnel the tunnel noise on the centerline is attributed to high vorticity in the wake of the fast acting valve [41]. Transition, more precisely heating augmentation, was only obtained for applied roughness and under forced freestream disturbance conditions illustrated by the "rough & in wake" distribution. This finding agrees well with the conclusions in Ref. [42] where also vorticity was found to be responsible for heating augmentation.

It can be concluded that the transition scenario reported in Ref. [26] and reproduced in Ref. [24] cannot explicitly be attributed to distributed surface roughness or freestream vorticity. The prevailing mechanism, if existent, and how it is amplified remain to be clarified. To investigate the local interaction of roughness and vortical freestream disturbances, direct numerical simulations (DNS) of the supersonic flow around the generic blunt Apollo type re-entry capsule in Ref. [24] are performed. Then, the findings of a clean configuration, i.e., smooth capsule and unperturbed freestream, are compared to the results of a configuration with distributed surface roughness, a clean configuration

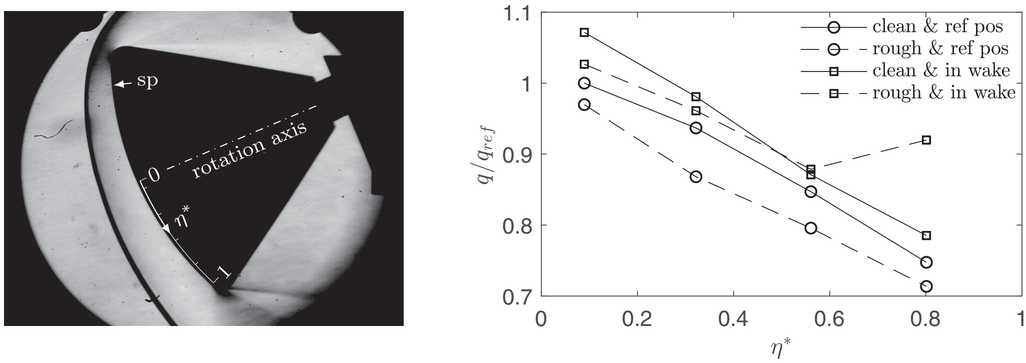

(a) (b)

FIG. 1. Apollo type re-entry capsule experiments by Radespiel *et al.* [24]: (a) Schlieren image of the wind tunnel experiment, "sp" denotes the stagnation point; (b) measured heat flux distributions q of four flow configurations. The notation "clean" and "rough" refers to the surface of the capsule while "ref pos" and "in wake" denote the position of the capsule in the wind tunnel. The η^* coordinate is defined in (a) and the reference heat flux q_{ref} is the first data point of configuration "clean & ref pos."

undergoing freestream streamwise vorticity disturbances, and finally, a rough-surface configuration plus vorticity perturbations. Furthermore, the effects of roughness type, Reynolds number, and vorticity intensity are investigated. Considering the different types of distributed roughness in Refs. [24,26], i.e., stochastic surface imperfections and deterministic roughness based on distributed elements, the following hypothesis is posed and challenged throughout the investigation. If various deterministic roughness distributions cause identical flow phenomena, stochastic roughnesses may be represented by deterministic roughnesses in numerical simulations and controlled experiments.

Note that first, based on the requirements of the physical problem modifications to the numerical method presented in Ref. [43] are discussed. Then, the numerical investigation on the receptivity of the capsule boundary layer to distributed roughness and the subsequent disturbance growth corresponding to the experiments in Ref. [24] is presented.

The paper is organized as follows. First, the numerical method is presented in Sec. II. Then, the computational setup of the capsule simulations is given. The results of the numerical simulations are presented in Sec. IV, before the essential findings are discussed in Sec. V.

II. NUMERICAL METHOD

The analysis of the micro roughness induced boundary layer disturbances defines a typical multiscale problem in mechanical engineering. The largest scale $\mathcal{O}(1)$ is given by the capsule diameter and determines the inviscid flow. The boundary layer thickness introduces a length scale of $\mathcal{O}(10^{-2})$ depending on the Reynolds number. Structured multiblock grids can be used to efficiently compute such flows [26]. The roughness height $\mathcal{O}(10^{-4})$ defines the smallest geometric scale. To resolve all scales, a finite-volume method using an unstructured Cartesian grid and cut cells, i.e., cells are cut by the surface and new interfaces for the flux balance are created [43], featuring intense local refinement is employed. To preserve conservation while refining the grid, special care must be taken to guarantee consistent surfaces for the flux balance of neighboring cut cells. This conservation is guaranteed by the wall-mesh variation (WMV) approach for Cartesian cut-cell methods which will be discussed in detail in Sec. II B 1.

A. Governing equations

The numerical simulations are based on the nondimensionalized Navier-Stokes equations

$$\int_V \frac{\partial \mathbf{Q}}{\partial t} dV + \oint_A \overline{\mathbf{H}} \cdot \mathbf{n} dA = \mathbf{0}. \tag{1}$$

The quantity $\mathbf{Q} = [\rho, \rho\mathbf{u}^T, \rho E]^T$ is the vector of the conservative variables with the density ρ, velocity vector $\mathbf{u}$, and the total specific energy $E = e + \mathbf{u}^2/2$ containing the specific energy e. The flux vector $\overline{\mathbf{H}}$ can be decomposed into an inviscid $\overline{\mathbf{H}}^i$ and a viscous part $\overline{\mathbf{H}}^v$

$$\overline{\mathbf{H}} = \overline{\mathbf{H}}^i + \overline{\mathbf{H}}^v = \begin{pmatrix} \rho\mathbf{u}^T \\ \rho\mathbf{u}\mathbf{u} + \overline{\mathbf{I}}p \\ \mathbf{u}^T(\rho E + p) \end{pmatrix} + \frac{1}{\mathrm{Re}_0} \begin{pmatrix} \mathbf{0}^T \\ \overline{\boldsymbol{\tau}} \\ (\overline{\boldsymbol{\tau}}\mathbf{u} + \mathbf{q})^T \end{pmatrix}. \tag{2}$$

The Reynolds number is computed using the fluid properties at rest $\mathrm{Re}_0 = \rho_0 a_0 l_{\mathrm{ref}}/\eta_0$ indicated by the subscript "0." The quantity a denotes the speed of sound and l_{ref} is the characteristic length. The dynamic viscosity η is calculated using Sutherland's law. Furthermore, the volume viscosity is assumed to be zero such that the stress tensor for a Newtonian fluid $\overline{\boldsymbol{\tau}}$ can be written

$$\overline{\boldsymbol{\tau}} = \tfrac{2}{3}\eta(\nabla \cdot \mathbf{u})\overline{\mathbf{I}} - 2\eta[\nabla\mathbf{u} + (\nabla\mathbf{u})^T]. \tag{3}$$

The vector of heat conduction $\mathbf{q}$ is formulated according to Fourier's law

$$\mathbf{q} = -\frac{\lambda}{\mathrm{Pr}(\gamma - 1)} \nabla T \tag{4}$$

using the gradient of the static temperature ∇T, the thermal conductivity λ, the ratio of specific heats γ, and the Prandtl number $\mathrm{Pr} = \eta_\infty c_p/\lambda_\infty$, where c_p is the specific heat at constant pressure. The values for γ and Pr at air flow are $\gamma = 1.4$ and $\mathrm{Pr} = 0.72$. The system of equations is closed by the equation of state for an ideal gas

$$e = \frac{p}{\rho(\gamma - 1)}. \tag{5}$$

B. Discrete formulation

The domain is discretized by an unstructured hierarchical Cartesian grid [44]. During the grid generation, an initial Cartesian cell containing the entire computational domain is successively refined to yield the final grid. The refinement is quantified in levels, i.e., whenever a cell is refined, the level of refinement is increased by one.

The boundaries of the computational domain are prescribed by triangulated surfaces [stereolithography format (STL)]. Local grid refinement can be created by two methods. First, boundary refinement can be applied by specifying a boundary STL to be refined. Second, several refinement patches defined by generic shapes, e.g., two points for a rectangle, can be prescribed.

On the resulting grid, the governing equations are integrated using a finite-volume method employing cut cells to represent the immersed boundary [45,46]. For the spatial discretization an advection upstream splitting method (AUSM) is used. In this method, the advection Mach number on the cell surface is the mean of the extrapolated Mach numbers from the adjacent cells $\mathrm{Ma}_{1/2} = 0.5(\mathrm{Ma}_L + \mathrm{Ma}_R)$. The same formulation holds for the pressure on the cell surface. The cell center gradients are computed using a second-order accurate least-squares reconstruction scheme [45]. Shock capturing is achieved by adding additional numerical dissipation at the shock position. Furthermore, small cut cells are treated using an interpolation and flux-redistribution scheme [43]. The temporal integration is based on a five-stage second-order accurate Runge-Kutta scheme.

Special care must be taken when the grid is refined in the direct vicinity of a curved boundary, i.e., the discretized representation of the boundary by the cut cells differs between neighboring cells of varying level of refinement. To align the representation, the cut cells have to be adapted

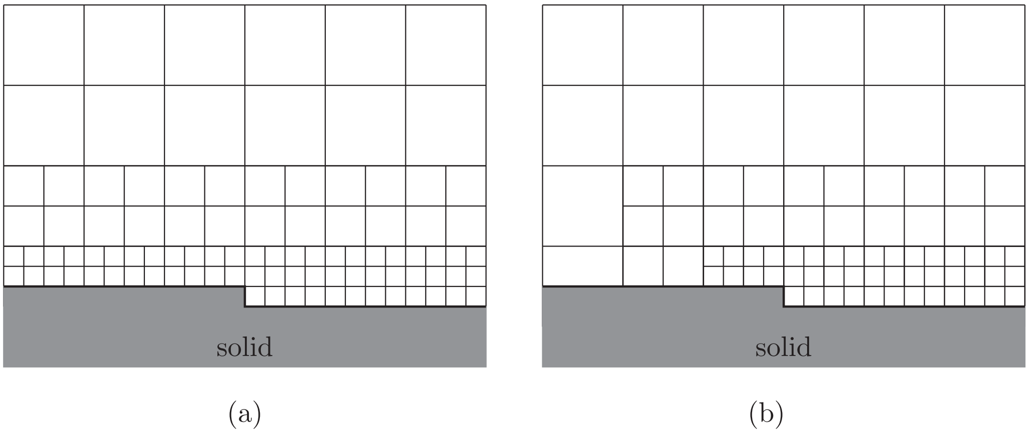

FIG. 2. Cartesian hierarchical meshes without WMV (a) and with WMV (b).

in a preprocessing step prior to the creation of any surface of the finite-volume method. Next, the concept of the WMV approach is thoroughly discussed.

1. Wall-mesh variation approach for Cartesian cut cell methods

First, the problem of maintaining conservativeness is discussed which occurs when WMV is used in Cartesian cut cell based flow solvers. Then, a method, which remedies this problem, and its implementation into the flow solver are presented.

To significantly reduce the total number of grid cells and the computational cost of a numerical simulation, the variation of the wall-mesh resolution along complex geometries is an extremely promising concept. A simple example to illustrate the meaning of wall-mesh variation is shown in Fig. 2 where the geometry over a backward-facing step is depicted. While in Fig. 2(a) the cell size in the streamwise direction near the wall does not change, the near-wall mesh in Fig. 2(b) is refined in the step region. Note that in two-dimensional problems and for geometries without any curvature such a mesh variation does not cause any problem whatever cut-cell concept is used. As discussed in the following, this is completely different when three-dimensional flows over curved bodies are considered in a cut-cell approach with a linearized geometry.

The spatial discretization of a curved geometry is conducted by linearly approximating its surface using the intersection points of the geometry with the edges of the Cartesian grid cells located on the boundary. When the grid is refined along the geometry, depending on its curvature cells of different size may have a different number of intersection points. The finer cells may have more intersection points posing a problem on the interface between two refinement levels. The shapes of the resulting faces on the interface and as such the connected areas are not identical especially in regions with high curvature of the geometry.

Figure 3 shows an interface between two different refinement levels, where the real geometry (top left) and the linearized geometry (top right) are illustrated. Furthermore, referring to the bottom illustrations in Fig. 3, cut points created by the intersection with the STL geometry are indicated by capital letters A_i, B_i, etc., for the finer cells and $\widetilde{A}_i$, $\widetilde{B}_i$, etc., for the coarser cell. The subscript i denotes the faces 1, 2, and 3. At the interface 2, two cut faces are created, the cut face of the coarse mesh with only two cut points, $\widetilde{A}_2$ and $\widetilde{B}_2$, and the cut face generated by the finer cells with three cut points, A_2, B_2, and C_2. This leads to a gap on the interface indicated in Fig. 3 (top right).

Due to the gap the conservation of mass, momentum, and energy is no longer ensured. Furthermore, the gap on the interface causes numerical errors during the simulation which can result in divergence of the solution procedure. To obtain fully conservative fluxes and to reduce the

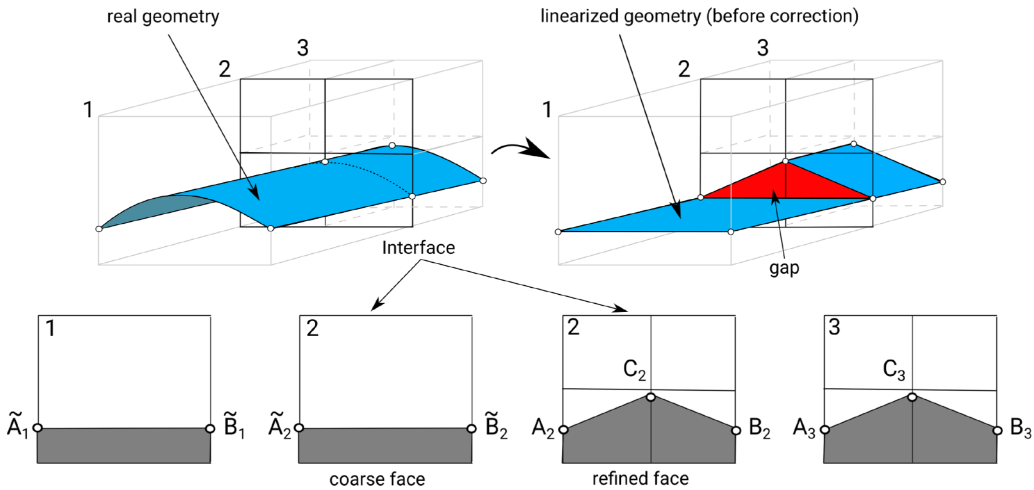

FIG. 3. Boundary refinement with WMV along a curved geometry (top left) and the linearized geometry before the cut-point correction (top right); cut points of faces 1, 2, and 3 created by the intersection with the STL geometry on the interface between two refinement levels without treatment (bottom).

numerical errors on the interface between two refinement levels a special treatment of the cut points is necessary.

The objective of the cut-point correction is to close the gap on the interface of two refinement levels by changing the fine-cell cutting such that the fluxes are conserved. Instead of using the intersection points of the STL geometry, the cut points of the finer cells on the interface are approximated by the cut points of its coarser neighbor cell. In Fig. 4 (bottom), the line that connects the cut points A_2 and B_2 is used to compute the new cut point C_2' which replaces the old cut point C_2. Depending on the curvature of the geometry more than one cut point, e.g., C_2, D_2, and E_2 in Fig. 5, has to be corrected on the interface. The linearized geometry after the cut point correction

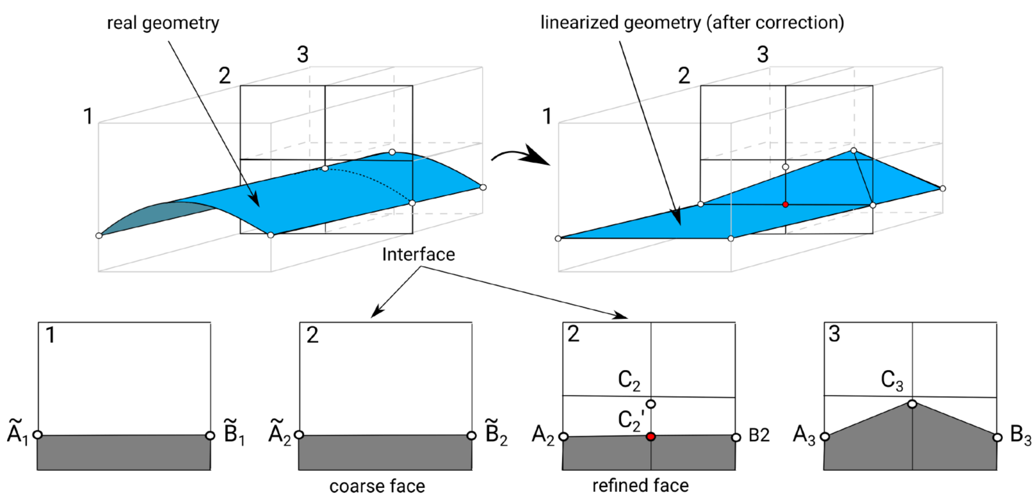

FIG. 4. Boundary refinement with WMV along a curved geometry (top left) and the linearized geometry after the cut-point correction (top right); corrected cut points of faces 1, 2, and 3 created on the interface between two refinement levels (bottom).

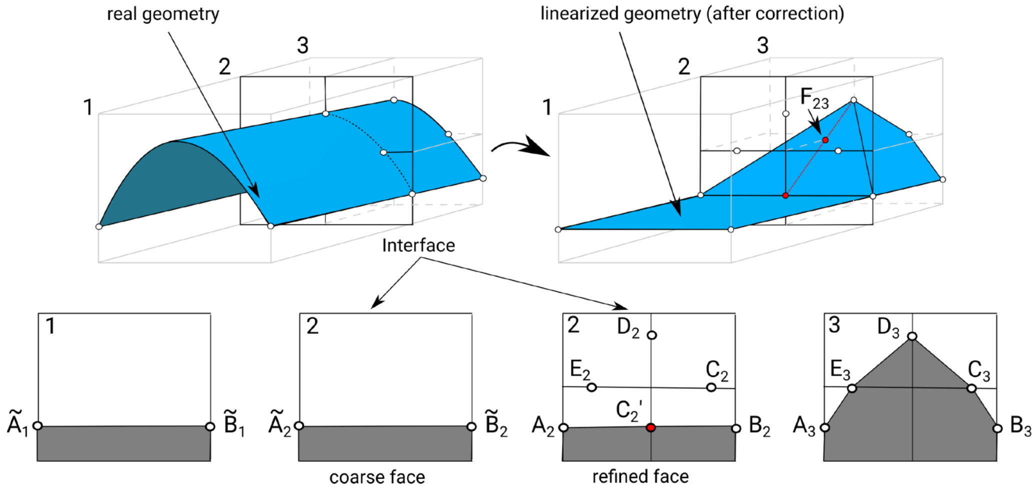

FIG. 5. Boundary refinement with WMV along a curved geometry (top left) and the linearized geometry after the cut-point correction (top right); corrected cut points of faces 1, 2, and 3 created on the interface between two refinement levels (bottom); example of a cutting case where an additional cut point F_{23} is inserted.

is depicted in Fig. 4 (top right). In certain cases, the correction of the cut points according to the coarser neighbor cell requires the generation of new boundary cells which are not intersected by the STL geometry but are cut by the corrected geometry. On the other hand, it can be necessary to remove boundary cells which intersect the STL geometry but are no longer cut by the corrected geometry, as explained in the following seven-step algorithm.

2. *Wall-mesh variation algorithm*

(i) *Label WMV boundary cells.* Cells intersecting the geometry described by the STL are labeled as boundary cells. In a first step, all boundary cells which are located on the interface between two refinement levels are identified. This is done by taking advantage of the hierarchical structure of the Cartesian mesh and the way neighbor cells are linked, since only equal level neighbors are stored. A boundary cell located on the interface can easily be identified by checking the neighbor information in all directions. A boundary cell that does not have any neighbor in a certain direction which, however, has a parent cell with a neighbor in this direction is marked.

(ii) *Identify cut points.* Cut points from the intersection with the STL geometry from the coarser cell $\widetilde{A}_i$, $\widetilde{B}_i$, etc., and from the finer cells A_i, B_i, etc., are computed and stored.

(iii) *Remove nonidentical cut points.* Cut points at the interface are compared. Cut points on the edges of the finer cells which do not exist at coarser cells, i.e., there is no corresponding edge of the coarser cell as for C_2 in Fig. 4 (bottom), are removed.

(iv) *Interpolate new cut points.* The remaining cut points, i.e., A_2 and B_2 in Fig. 4 (bottom) are linearly connected and a new cut point, i.e., C_2', is computed from its intersection with the cell edges of the finer cells on the interface. Depending on the location of A_2 and B_2 up to two new cut points have to be created on the interface.

(v) *Add intermediate cut points.* When the new cut points on the interface are computed, it can be necessary to create an additional cut point off the interface 2 as illustrated in Fig. 5. In this case five cut points are generated on the interface for the cut face of the finer cells, i.e., A_2, B_2, C_2, D_2, and E_2. The cut points C_2, D_2, and E_2 differ from the cut points on the cut face of the coarser cell and are therefore removed. The new cut point C_2' is generated by a linear connection of A_2 and B_2. Since the cut point C_2' cuts the two lower cells and the cut point D_3 exists on face 3, which cuts the two upper cells, an additional cut point F_{23}, which cuts all four cells and is located between face

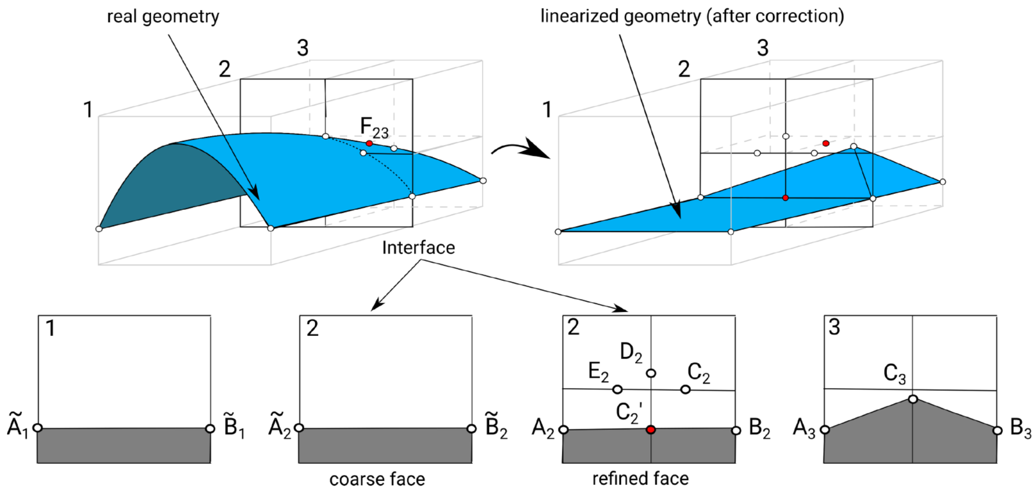

FIG. 6. Boundary refinement with WMV along a curved geometry (top left) and the linearized geometry after the cut-point correction (top right); corrected cut points of faces 1, 2, and 3 created on the interface between two refinement levels (bottom); example of a cutting case where former boundary cells are no longer cut after the cut-point correction; these cells are removed from the list of boundary cells.

2 and 3, is necessary. This cut point is placed in the center of the corresponding edge as shown in Fig. 5 (top right).

(vi) *Add or remove boundary cells.* If a cell is no longer cut after the cut-point correction, it has to be removed from the list of boundary cells. An example is shown in Fig. 6, where the old cut points on the interface C_2, D_2, and E_2 cut the upper cells and the cut point C_3 on face 3 cuts the lower cells. Therefore, a cut point F_{23} exists between face 2 and face 3 in Fig. 6 (top left) before the cut-point correction. After the cut-point correction, the new cut point C_2' in Fig. 6 (bottom) is positioned at the lower cells, the cut point F_{23} has to be removed, and the upper cells are no longer cut. These cells are removed from the boundary cell list. The opposite case, i.e., a cell which is not cut before but after the cut point correction and then a new cell has to be added to the list of boundary cells is also possible and has to be considered.

(vii) *Define final cut-cell distribution.* In a final step, the cells are cut by the new cut points and the part of the cells which are located inside the fluid region are kept whereas the other part of the cells is deleted.

Since the cut cells also depend on the neighboring cells, the WMV setup is not a local operation in massively parallel simulations. Therefore, after the seven steps are completed on internal cells of the various computational subdomains, the determined cut points need to be communicated to the corresponding halo cells required for the flux computation across subdomain boundaries [44]. The overhead which is introduced by the cut-point correction in terms of memory and computing time is negligible.

III. COMPUTATIONAL SETUP

First, the dimensions of the Apollo type re-entry capsule and the distributed roughness are described. Then the computational domain and the grid are presented.

A. Apollo type re-entry capsule and distributed roughness

The dimensions of the capsule forebody used in Refs. [24,26] are shown in Fig. 7(a). The main part of the forebody is spherical with a radius of $R = 204.1$ mm and an opening angle of $\Theta = 46^{\circ}$.

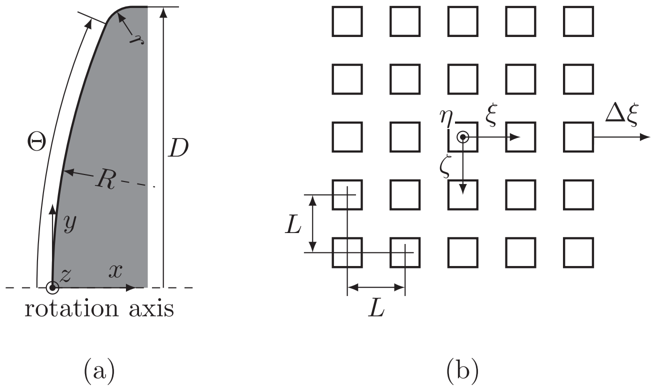

FIG. 7. Computational setup: (a) schematic of the smooth axisymmetric capsule, the opening angle of the spherical forebody of radius $R = 204.1$ mm is $\Theta = 46^\circ$, its diameter is $D = 170$ mm, the smooth contour exhibits a capsule shoulder radius of $r = 8.5$ mm; (b) schematic of the aligned distributed roughness, the spacing between the elements is $L = 200\ \mu$m; (c) schematic of the staggered distributed roughness, the second and fourth row of elements are reduced by one element and misaligned in the ζ direction by $L/2$.

Toward the outer diameter of $D = 170$ mm, the cap smoothly transitions into a rounded shoulder with radius $r = 8.5$ mm. The origin of the $\mathbf{x} = (x, y, z)^T$ coordinate system is located in the center of the spherical part of the forebody. The freestream flow $\mathbf{u}_\infty$ lies in the x-y plane and is $\mathbf{u}_\infty = u_\infty(\cos\alpha, \sin\alpha, 0)^T$, α defines the angle of attack.

The geometry of the distributed roughness is illustrated in Figs. 7(b) and 7(c). They are located on the rotation axis of the capsule in Fig. 7(a). On the capsule surface, the $\boldsymbol{\xi} = (\xi, \eta, \zeta)^T$ coordinate system is used. The streamwise direction at the boundary layer edge is ξ. The wall normal coordinate is η and ζ denotes the azimuthal direction. In the center of the $\mathbf{x}$ coordinate system, y coincides with ξ, $\eta = -x$, and $\zeta = z$, i.e., the streamwise flow direction at the boundary layer edge in Figs. 7(b) and 7(c) is from left to right. Furthermore, it is shown in Fig. 7(b) that streamwise distances with respect to the end of the last row of elements are denoted $\Delta\xi$.

Each of the distributed roughnesses consists of a certain number of identical single roughness elements having a square base of $100 \times 100\ \mu\text{m}^2$. Two patterns are considered the location of which on the surface of the capsule is defined in Sec. III B. In Fig. 7(b) the "aligned" configuration with 5×5 elements is depicted. This configuration possesses unblocked passages between the columns of elements. The spacing between the elements is $L = 200\ \mu$m. The "staggered" configuration is shown in Fig. 7(c). The second and fourth row of elements are reduced by one element and misaligned in the z direction by $L/2$. The projected area in the y direction is without any gaps. The base area of both patches is $0.9 \times 0.9\ \text{mm}^2$. All roughness elements protrude 20 μm into the boundary layer.

The roughness in Fig. 7(b) corresponds to the layout of the corresponding experiments in Ref. [24]. For computational reasons, that will be elaborated on in the next section, the numerical setup has less elements than the experimental counterpart. That is, in the experiments 100×100 elements are applied on the capsule forebody. To address the difference between the setups, i.e., the finiteness of the roughness distribution, a single rectangular element is included in the analysis. It covers the complete base area of $0.9 \times 0.9\ \text{mm}^2$ and is referred to as "single."

B. Computational domain and boundary conditions

A schematic of the computational domain and the boundary conditions is depicted in Fig. 8. On the upstream boundary "in" supersonic Dirichlet conditions are prescribed for all variables. This boundary is located just upstream of the detached shock wave whose location is determined in a

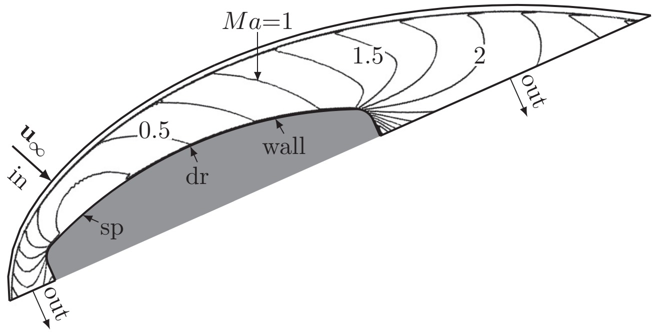

FIG. 8. Computational domain including lines of constant Mach number. "in" denotes the Ma = 5.9 supersonic inflow boundary at an angle of attack of $\alpha = 24^\circ$, "out" defines supersonic outflow, and at the "wall," no-slip and a constant temperature of 295 K are prescribed. "sp" represents the stagnation point at $y/D = 0.356$ of the rotation axis. "dr" denotes the location of the distributed roughness.

prior simulation. On the outflow boundary "out" supersonic outflow von Neumann conditions for all variables are imposed. The capsule wall is modeled as a no-slip isothermal wall with a wall temperature of 295 K. The isothermal condition is justified by the short runtime of the wind tunnel of about 80 ms [41].

As aforementioned, the computational grid features various regions of local refinement using the wall-mesh variation approach. These regions are indicated in Fig. 9. Figure 9(a) shows the forebody of the capsule limited to about 25% of the azimuthal extent. The stagnation point is denoted by "sp" and the roughness patch is located at $\mathbf{x} = \mathbf{0}$. Obviously, most of the capsule boundary layer, e.g., the azimuthal extent $|z|/D > 0.05$, can be considered less relevant for the analysis of the receptivity of the boundary layer to the roughness. Therefore, these regions are deliberately considered less important for the grid design. The properties of the local boundary layer at the roughness location have to be verified, i.e., a validation of the local boundary layer will be shown.

The ellipse in Fig. 9(a) "bl refinement" encloses the first region of the local boundary refinement to resolve the boundary layer. It starts half-way between the stagnation point and the roughness area. In Fig. 9(b), a cross section in the y-z plane ($\xi - \eta$) at $z = 0$ is shown, i.e., the local flow is from left to right as indicated by the boundary layer velocity profile "bl." The uppermost line represents the wall normal border of the local boundary refinement and contains the entire boundary layer "bl." The grid in the vicinity of the roughness at $\mathbf{x} = \mathbf{0}$ (not shown in Fig. 9(a)) is further refined using patch refinement. In Fig. 9(a), only the outermost patch out of three patches is shown. Further rectangular patches are shown in Figs. 9(b) and 9(c). Note that Figs. 9(b) and 9(c). are scaled by a factor 80 with respect to Fig. 9(a) and the cells "cells" and the boundary layer are to scale. The roughness centered at $\mathbf{x} = \mathbf{0}$ is represented by the aforementioned configuration "single." The overall grid size, including some general refinement toward the capsule surface and the shock wave, is 300 million cells. The boundary layer refinement contains 60 million and the rectangular patches consists of 32 million cells. Note that these regions of refinement requiring 30% of the cells only account for a tiny fraction of the computational domain, i.e., the refined boundary layer covers approximately 1% of the computational domain and the 32 million cells in the vicinity of the roughness account for 6.5×10^{-5}%. Implementing the 100×100 elements applied in the experiments requires at least additional 6 billion grid cells.

To emphasize the importance of WMV and support the grid topology, some comparative numbers are given. If the ellipse of the boundary layer refinement is extended to include the entire capsule, only the number of cells required to resolve the boundary layer rise to 5 billion. Keeping the innermost rectangle refinement patch at a minimum height over the entire capsule, 14 billion cells

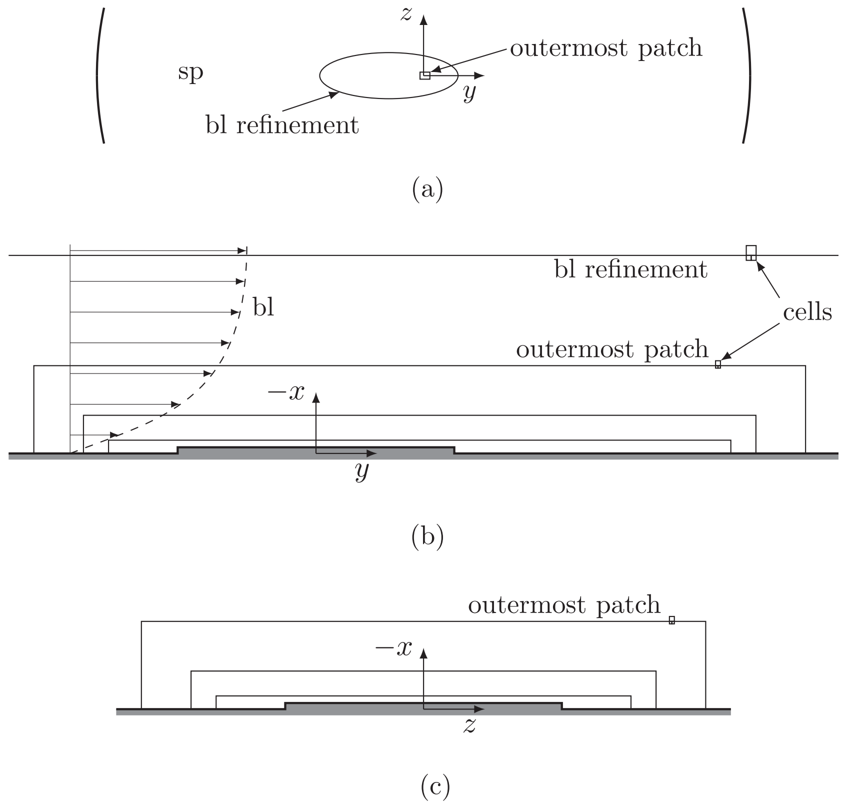

FIG. 9. Grid topology of the capsule simulations: (a) front view of the capsule, “sp” denotes the stagnation point, the ellipse “bl refinement” encloses the region of local boundary refinement, and the rectangle “outermost patch” is the front view of the outermost rectangle refinement patch shown in the subfigures below; (b) detailed view of cross section showing the wall normal and streamwise dimensions of the rectangle refinement patches in the vicinity of the roughness, scaling factor 80, boundary layer “bl” and cells are to scale; (c) detailed view of cross section showing the wall normal and azimuthal extent of the refinement patches, scaling factor 80.

are generated. To circumvent the resulting computational humungous effort for single simulations, let alone parameter variations, WMV has to be used to restrict the computational effort to the regions of interest.

IV. RESULTS

Before the results are presented, the various cases are outlined. All the configurations of the DNS are summarized in Table I. First, the unperturbed flow over the smooth capsule is computed for three Reynolds numbers using the grid presented in Sec. III B. These solutions serve as reference for the perturbations induced by the roughness. They are denoted cases No. 1 to 3 in Table I. Then, the three roughness configurations, i.e., aligned, staggered, and single, are defined by cases 4 to 9 to investigate the receptivity of the boundary layer and the subsequent streamwise development of the disturbances at the lowest and highest Reynolds number.

Compared to the measurements in Ref. [24], the unit Reynolds numbers linked to the Reynolds numbers in Table I are $\mathrm{Re}_L/D = 6.25 \times 10^6\ \mathrm{m}^{-1}$, $\mathrm{Re}_M/D = 12.5 \times 10^6\ \mathrm{m}^{-1}$, and $\mathrm{Re}_H/D = 18 \times 10^6\ \mathrm{m}^{-1}$. In the experiments, cases 1, 3, 4, and 5 were investigated.

TABLE I. Flow configurations and parameters: Reynolds number $\mathrm{Re} = \rho_\infty u_\infty D/\eta_\infty$ with $\mathrm{Re}_L = 1\,062\,500$, $\mathrm{Re}_M = 2\,125\,000$, and $\mathrm{Re}_H = 3\,060\,000$; roughness type with "aligned" depicted in Fig. 7(b) "staggered" in Fig. 7(c), and "single" denotes a single element having the same extent as the distributed roughnesses. Constant parameters throughout are the freestream Mach number $\mathrm{Ma} = 5.9$, freestream total temperature $T_0 = 470$ K, wall temperature $T_w = 295$ K, and the angle of attack 24°.

	Smooth	Aligned	Staggered	Single
Re_L	1	4	6	8
Re_M	2	–	–	–
Re_H	3	5	7	9

A. Unperturbed flow

The unperturbed boundary layer of the clean configuration is compared to numerical results from Ref. [26]. The reference DNS of the unperturbed flow were the basis for stability analyses. The solutions are validated by experimental heat flux data on the entire capsule forebody. Therefore, instead of validating the current solutions versus the experimental surface heat flux data, the former numerical boundary layer data from Ref. [26] are considered for the validation. Figure 10 shows a comparison of the velocity and temperature boundary layer distributions at the position of the later

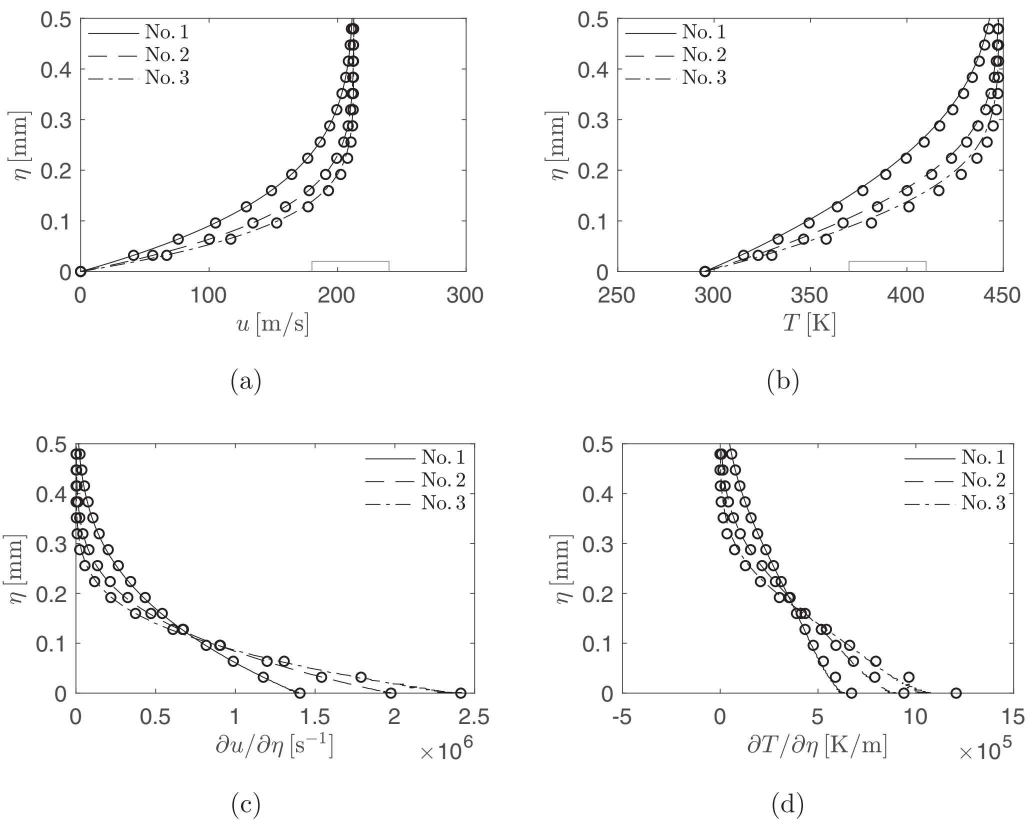

FIG. 10. Validation of the simulated boundary layers of the smooth capsule configuration at the location of the roughness, i.e., at $\mathbf{x} = \mathbf{0}$, for the three Reynolds numbers in Table I. The circles "∘" denote the data from the present simulations and the lines denote corresponding data from Theiss *et al.* [26].

TABLE II. Properties of the unperturbed boundary layers: Reynolds number Re_{δ^*} based on the displacement thickness δ^* and boundary layer edge values; Reynolds number Re_Θ based on the momentum thickness Θ and the boundary layer edge values; boundary layer thickness δ at 99.5% of the freestream total enthalpy; roughness Reynolds number Re_{kk} based on the roughness height $k = 0.02\ \mu$m and the fluid properties at $\eta = k$ of the unperturbed boundary layer, for $\mathrm{Re}_{kk,w}$, the kinematic viscosity at $\eta = 0$ is used; velocity u_e, temperature T_e, density $\rho_{e,i}$, and Mach number Ma_e at the boundary layer edge. For the density, i refers to the No. in the upper table.

No.	Re_{δ^*}	Re_Θ	δ (μm)	δ^* (μm)	Θ (μm)	$\mathrm{Re}_{kk}(\mathrm{Re}_{kk,w})$	k/Θ
1	109	83	548	88.8	67.8	5.82(6.02)	0.295
2	152	116	383	62.3	47.5	15.6(16.3)	0.421
3	181	134	295	51.3	38	26.3(27.9)	0.526
u_e (m/s)	T_e (K)	$\rho_{e,1}$	$\rho_{e,2}$	$\rho_{e,3}$ (kg/m^3)	Ma_e		
212	445	1.43	2.85	4.1	0.5		

added roughness, i.e., the axis of rotation. The velocity component parallel to the wall u and its derivative in the normal direction $\partial u/\partial \eta$ agree well with the reference data. At the highest Reynolds number, small deviations occur. The temperature distributions in Figs. 10(b) and 10(d) show a small deviation toward a somewhat fuller profile. Overall, we consider the boundary layer at the location of the roughness in the present simulations to be in good agreement with the simulations in Ref. [26] and the experiments in Ref. [24].

Integral values of the unperturbed boundary layers are summarized in Table II. At the highest Reynolds number, the ratio of roughness height k and momentum thickness Θ is closest to the range of k/Θ being related to boundary layer transition induced by transient growth [24]. The effect of the surface roughness on the boundary layer is shown next.

B. Disturbance energy

The development of disturbances in perturbed flows can be quantified using the energy norm derived by Mack [16] and Hanifi *et al.* [47]. Deviations from the unperturbed velocity $\mathbf{u}'$ and thermodynamic state (ρ', T') contribute to the total disturbance energy $\boldsymbol{\sigma}\cdot\boldsymbol{\sigma}$ defined by

$$\boldsymbol{\sigma}(\boldsymbol{\xi}) = \left(\sqrt{\frac{\overline{T}}{\overline{\rho}}\frac{\rho_{\mathrm{ref}}}{T_{\mathrm{ref}}}\frac{1}{\gamma \mathrm{Ma}_{\mathrm{ref}}^2}}\frac{\rho'}{\rho_{\mathrm{ref}}}, \sqrt{\frac{\overline{\rho}}{\rho_{\mathrm{ref}}}}\frac{\mathbf{u}'^T}{u_{\mathrm{ref}}}, \sqrt{\frac{\overline{\rho}}{\overline{T}}\frac{T_{\mathrm{ref}}}{\rho_{\mathrm{ref}}}\frac{1}{\gamma(\gamma-1)\mathrm{Ma}_{\mathrm{ref}}^2}}\frac{T'}{T_{\mathrm{ref}}}\right)^T. \tag{6}$$

The overbar denotes quantities of the unperturbed flow. This energy norm is commonly used in analyses of optimal perturbations in compressible boundary layers for maximum disturbance growth using the linearized Navier-Stokes equations [23,32,34,48]. The reference values "ref" are taken from the boundary-layer edge. To obtain the disturbance energy of a structure, $\boldsymbol{\sigma}\cdot\boldsymbol{\sigma}$ is integrated in space. The components of the integrated disturbance energy $\mathbf{E}$ in a $\zeta-\eta$ slice at constant ξ read

$$\mathbf{E}(\xi) = \int_{-\infty}^{\infty}\int_0^{\infty} \mathrm{PSD}_\zeta[\boldsymbol{\sigma}(\boldsymbol{\xi})]d(\eta/\delta)d(\beta/\beta_{\mathrm{ref}}) \tag{7}$$

using the azimuthal power-spectral density PSD_ζ. Since only azimuthal PSDs are considered, the subscript is omitted in the following. Computing PSDs at constant ξ yields the wall normal distribution of disturbance energy in the wave-number space. Spatial integration of the wall normal distribution results in the disturbance energy of an entire $\zeta-\eta$ slice in the wave-number domain. The final integration over β reduces the flow disturbances to the components of the integrated disturbance energy $E = \sum_i E_i$. The sum of the components of $\mathbf{E}$ related to the velocity perturbations are denoted kinetic disturbance energy E_{ki} and the sum of the components defined by the thermodynamic state is E_{st}, i.e., $E = E_{ki} + E_{\mathrm{st}}$. This nomenclature also holds for PSDs of $\boldsymbol{\sigma}$, e.g., $\mathrm{PSD}(\sigma_{ki}) = (0, 1, 1, 1, 0)^T \cdot \mathrm{PSD}(\boldsymbol{\sigma})$. Furthermore, $\mathrm{PSD}(\sigma) = (1, 1, 1, 1, 1)^T \cdot \mathrm{PSD}(\boldsymbol{\sigma})$ is defined. Whenever phase information is important, coefficients of fast Fourier transformations (FFT) are shown. Flows over rough surfaces, i.e., cases 4 to 9, are presented next.

C. Perturbed flow

The roughness induced perturbations of the experiments in Ref. [24] are presented. The sensitivities to Reynolds number, roughness layout, and roughness extent are investigated. The analysis is subdivided into the following steps. First, the initial flow displacement downstream of the distributed roughness is analyzed in the physical domain and the intensity of the perturbations in the wake are evaluated. Then, the initial disturbance field is scrutinized in the wave-number domain to identify the most relevant spectral components. Next, the disturbance energy is analyzed to quantify transient growth before the underlying mechanism is outlined. Finally, the disturbance fields and growth computed in the DNS are compared to results of optimal transient growth theory.

1. *Wake topology in the physical domain*

The topology of the flow perturbation imposed by the distributed roughness can be characterized by, e.g., the streamwise mass flow deficit $m' = (\rho u)'$ in the vicinity of the elements. Figure 11 shows the mass flow deficit in the ζ-η plane at $\Delta\xi = 0.05$ mm downstream of the distributed roughness. At negative values of ζ, the data of the staggered configuration is shown whereas for positive ζ, the aligned flow field is depicted. Figure 11(c) shows the data of Fig. 11(a) integrated in the wall normal direction. Furthermore, the data of case 8, i.e., the large single element, is included for comparison. A corresponding integration is shown in Fig. 11(d) for the higher Reynolds number.

The deviation from the unperturbed flow is due to two effects. First, disturbances related to single roughness elements occur close to the roughness elements. Second, the distributed but finite roughness appears as a large obstacle to the flow. That is, disturbances related to the length scale of the roughness elements develop inside the disturbance of the overall distributed roughness. For the lower Reynolds number, the differences between the aligned and staggered roughness are insignificant in Figs. 11(a) and 11(c). Differences can be observed in Figs. 11(b) and 11(d) for the higher Reynolds number. The misaligned elements reduce the local maxima at $\zeta = -0.1$ mm and $\zeta = -0.3$ mm. The aforementioned second effect is hardly affected.

The flow perturbation generated by the roughness is now modulated in the downstream direction. In linear transient growth theory, the ratio of disturbance energy $G = E_{\mathrm{out}}/E_{\mathrm{in}}$ defines the gain G of an arbitrary perturbation field and since the theory is linear, the amplitude of the initial perturbation distribution does not affect the gain. However, in the present simulations, the streamwise development of the perturbations is computed solving the nonlinear governing equations. Being a nonlinear product of streamwise velocity and density, the mass flow rate perturbations of cases No. 5, 7, and 9 are checked for linearity. In Fig. 12(a), the maximum mass flow rate deviation in each ζ-η plane is normalized and plotted versus the streamwise distance $\Delta\xi$. In close vicinity of the roughness, the perturbation is high but it decreases downstream. The error of the linear reconstruction of the perturbation m' in Fig. 12(a) is evaluated in Fig. 12(b). Even in close vicinity of the roughness, the linear expansion $m'_{\mathrm{lin}} = \overline{u}\rho' + \overline{\rho}u'$ gives good results with a relative error below 3%. Note that this is not a sound proof of the applicability of linear transient growth theory. This simple computation indicates the flavor of nonlinear effects due to roughness induced flow perturbations.

In the following, we switch from the analysis in the physical domain to the wave-number domain to identify the relevant spectral perturbation components in the wake.

2. *Wake topology in the wave-number domain*

The decomposition of the perturbation field of, e.g., Fig. 11(b), into the aforementioned scales will be based on PSDs or FFTs. However, before PSDs of the actual disturbances are presented, an

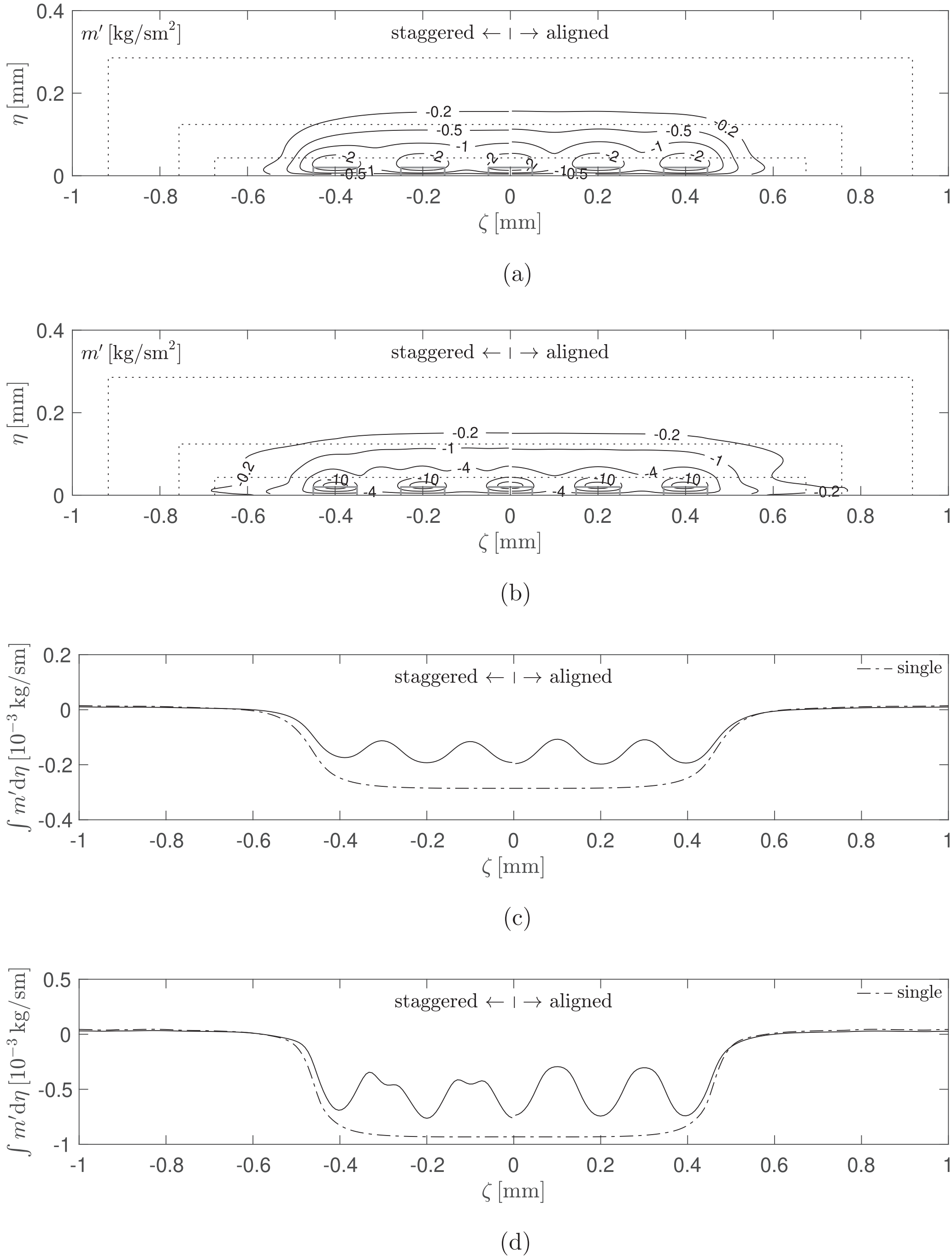

FIG. 11. Mass flow deficit of cases 4 to 9 in Table I at $\Delta\xi = 0.05$ mm downstream of the distributed roughness, at negative values of ζ, the data of the staggered configuration is shown whereas for positive ζ, the aligned flow field is depicted, the dotted lines in (a) and (b) indicate the grid refinement in Fig. 9(c): (a) lines of constant $m' < 0$ of cases Nos. 4 and 6, $\mathrm{Re_L} = 1\,062\,500$; (b) lines of constant $m' < 0$ of cases Nos. 5 and 7, $\mathrm{Re_H} = 3\,060\,000$; (c) integrated mass flow rate perturbation of Fig. 11(a) including data of the single configuration No. 8, $\mathrm{Re_L} = 1\,062\,500$; (d) integrated mass flow rate perturbation of Fig. 11(b) including data of the single configuration No. 9, $\mathrm{Re_H} = 3\,060\,000$.

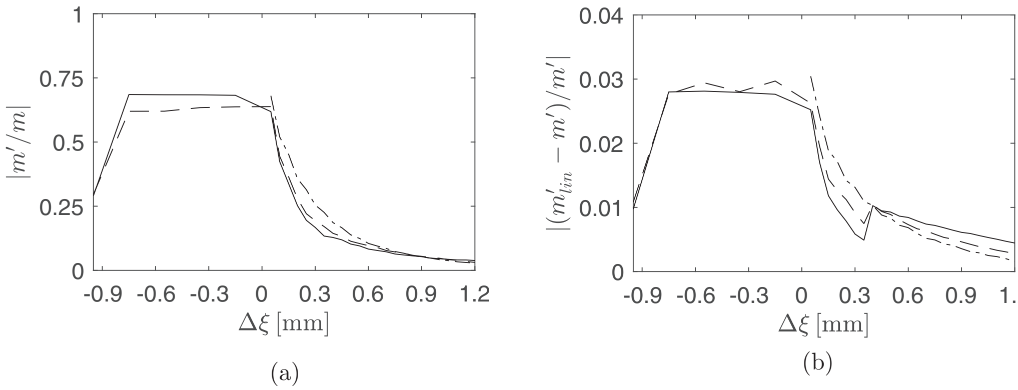

FIG. 12. Peak mass flow rate deviations in ζ-η planes (——aligned, - - - staggered, -·-·-single): (a) normalized using the local mass flow rate; (b) error of the m' reconstruction using the linear expansion $m'_{\text{lin}} = \overline{u}\rho' + \overline{\rho}u'$.

analytic representation of the last row of elements of distributed roughness in the wave-number domain for $n = 5$ and $n = 100$ elements is shown in Fig. 13. The former number of elements is defined by the DNS and rows of 100 roughness elements are installed on the capsule in the experiments in Ref. [24]. Given the different overall extent of the distributed roughness in the experiment and DNS, possible interactions of the disturbance components of the elements and the overall scale in the wave-number domain are scrutinized. Consider an azimuthal PSD at $\Delta\xi = 0$ and $\eta = k$ of the perturbation, e.g., streamwise velocity, mass flow rate, or temperature, at low order. In comparison to the flow over the smooth configuration, at the location of the elements the value is prescribed by the isothermal no-slip wall boundary condition on the protruding elements. Anywhere else the smooth wall boundary conditions are applied. The unchanged regions are represented by 0 and the perturbation by 1. The abscissa is scaled by the wave number of a single element $\beta_L = 2\pi/L$. The PSD of the distributed roughness is compared to the PSD of a single element of width $(n - 0.5)L$ denoted by "single" and the PSD of an infinite number of elements denoted by "∞" defined by a square wave oscillating between 0 and 1. The ordinate is scaled by the value

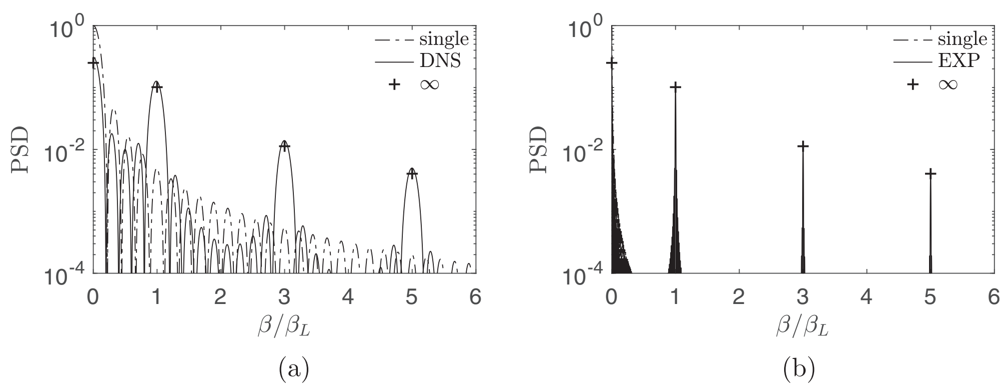

FIG. 13. Analytic representation of the last row of elements of distributed roughness in the wave-number domain using the PSD: (a) numerical configuration "DNS" of $n = 5$ elements; (b) experimental configuration "EXP" of $n = 100$ elements in Ref. [24]. The data denoted "single" assume a large element of $(n - 0.5)L$, whereas "∞" shows the PSD of an infinite number of elements, i.e., a square wave. The wave number is scaled by the wave number of a single element $2\pi/L$. The ordinate is scaled by the value of "single" at $\beta = 0$.

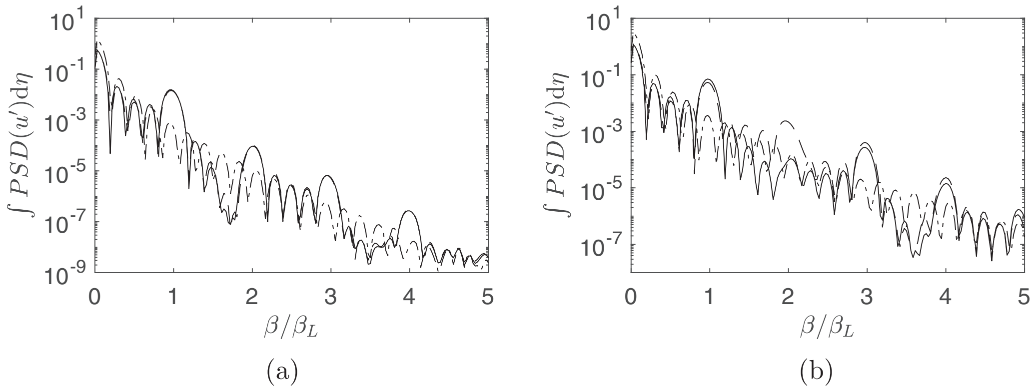

FIG. 14. PSD of the streamwise velocity perturbation (——aligned, - - - staggered, -·-·-single): (a) cases 4, 6, and 8, $\mathrm{Re_L} = 1\,062\,500$; (b) cases 5, 7, and 9, $\mathrm{Re_H} = 3\,060\,000$.

of the “single” case at $\beta = 0$ which denotes the projected area of the roughness in the ζ-η plane. For the numerical and experimental configuration in Figs. 13(a) and 13(b), the odd multiples of β_L have the same order of magnitude like the “∞” data. Furthermore, the perturbation related to the configuration “single” is one order of magnitude lower than the numerical setup and several orders than the experimental configuration with 100 elements. Between the odd multiples for $n = 5$, the finite extent of the distributed roughness causes minor peaks at odd multiples of the fundamental wave number $\beta_L/(2n - 1)$ of the single configuration. Although different in their azimuthal extent at odd multiples of the fundamental wave number β_L, the results of the DNS can be considered unaffected by the smaller extent in comparison with the experiments in Ref. [24]. Furthermore, the configuration “single” can be used to estimate the interference in the wave-number domain.

Figure 14 shows the wall normal integrated PSDs of the azimuthal distribution of the streamwise velocity perturbation. Compared to Fig. 13(a), the similarity of the pattern is evident. As expected for 5 elements, the impact of the individual elements acting as a single large element is apparent. At $\beta/\beta_L = 1$ and 3, the effect of the individual elements is one order of magnitude higher than the harmonics of the wave number $\beta/\beta_L = 1/9$ excited by the configuration “single.” For the lower Reynolds number in Fig. 14(a), the aligned and staggered configuration show almost identical velocity fluctuations corroborating the previous observation in Figs. 11(a) and 11(c). In contrast to Fig. 13, also even multiples of β_L show pronounced peaks. At $\beta = 2\beta_L$, for the higher Reynolds number in Figs. 14(b), the distributed roughnesses differ significantly. The suppression of the second harmonic of the aligned distribution at the higher Reynolds number is peculiar since the harmonic is present for the lower Reynolds number. This feature of the high Reynolds number flow is analyzed next using the wall normal distribution of FFTs at fixed wave numbers β_L and $2\beta_L$ in Fig. 15.

Since the flow is symmetric with respect to $\zeta = 0$, the perturbations of the streamwise velocity in Fig. 15(a) are proportional to $\pm\cos(\beta\zeta)$. The same holds for the wall normal velocity in Fig. 15(c). Finding the center of a roughness element in the last row of the distributed roughness at $\zeta = 0$, Fig. 15(a) shows a negative streamwise velocity perturbation in the wakes downstream of the elements. Next to these wakes, the displaced fluid forms positive streamwise velocity perturbations. The wall normal velocity perturbations in Fig. 15(c) denotes downwash downstream of the elements. The azimuthal velocity in Fig. 15(b) is proportional to $\pm\sin(\beta\zeta)$, i.e., the Fourier coefficients are imaginary, and is rotated onto the real axis by a multiplication with the imaginary unit $i = \sqrt{-1}$. Hence, the data in Fig. 15(b) shows convergent flow in the wakes behind the elements and diverging flow in between. The “single” data indicates an amplification of these effects due to the finite azimuthal extent of the distributed roughnesses since this effect is included in the FFTs downstream of these configurations.

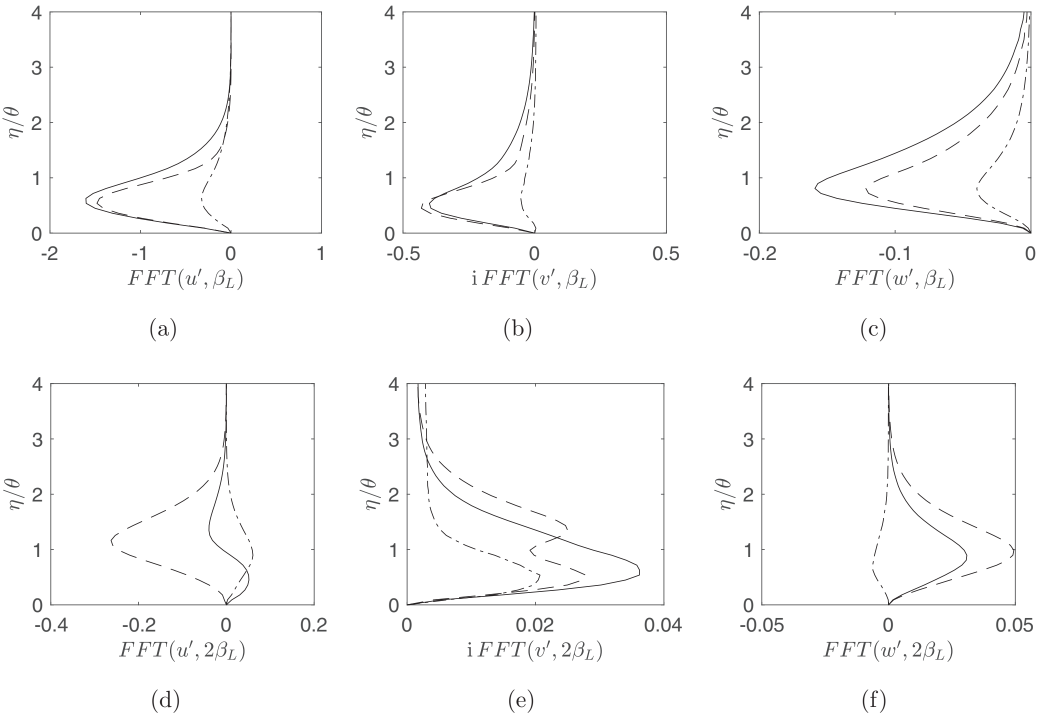

FIG. 15. Wall normal distribution of the velocity perturbation for cases No. 5, 7, and 9 at $\Delta\xi = 0.05$ mm downstream of the distributed roughness (——aligned, - - - staggered, -·-·-single): (a)–(c) fundamental wave number β_L; (d)–(e) second harmonic $2\beta_L$. The imaginary unit i in (b) and (e) denotes a phase shift of $\pi/2$ with respect to, e.g., the streamwise velocity perturbation.

The wall normal distribution of the streamwise velocity at $2\beta_L$ in Fig. 15(d) shows the reason for the differences in Fig. 14(b), i.e., the suppression of the harmonic at $\beta/\beta_l = 2$ for the experimental "aligned" configuration. The negative data for the staggered configuration causes the velocity deficit based on β_L to occur more cusp like in the physical domain and flattens the regions with locally increased velocity shown in Fig. 11(d). The disturbance does not constitute a plain harmonic of the fundamental perturbation but is explicitly generated, i.e., it occurs not before the first staggered row of elements and grows up to $\Delta\xi = 0.05$ mm. The disturbance for the aligned case is generated at the first row of elements and shows a pronounced positive peak, i.e., peaky regions of positive and flat regions of negative velocity fluctuations. It monotonically decreases up to $\Delta\xi = 0.05$ mm. Evidence for both trends can be found in Fig. 17(d) for $\Delta\xi \leqslant 0.05$ mm discussing the development of the disturbance energy. In Fig. 15(e), the azimuthal velocity component at $2\beta_L$ is illustrated. All cases show a global maximum in the vicinity of the wall and the influence of the distributed roughness acting as a large obstacle is high. For $\eta/\theta > 1$, the staggered configuration possesses a unique further maximum. The wall normal velocity component at $2\beta_L$ in Fig. 15(f) shows only a minor contribution of the harmonic belonging to the full extent of the roughness. Clearly, the perturbations induced by the staggered roughness at $2\beta_L$ contribute more energy. The evaluation of the disturbance energy to show transient growth is presented next.

3. Quantification of transient growth

Figure 16 exhibits the disturbance energy components E_{ki} and E_{st} at $\Delta\xi = 0.05$ mm in the wave-number domain using PSDs of σ_{ki} and σ_{st}. The results in Fig. 16(a) reflect the previous observations from the analysis of the streamwise velocity since σ_{ki} contains u'. In general, the contribution of σ_{ki}

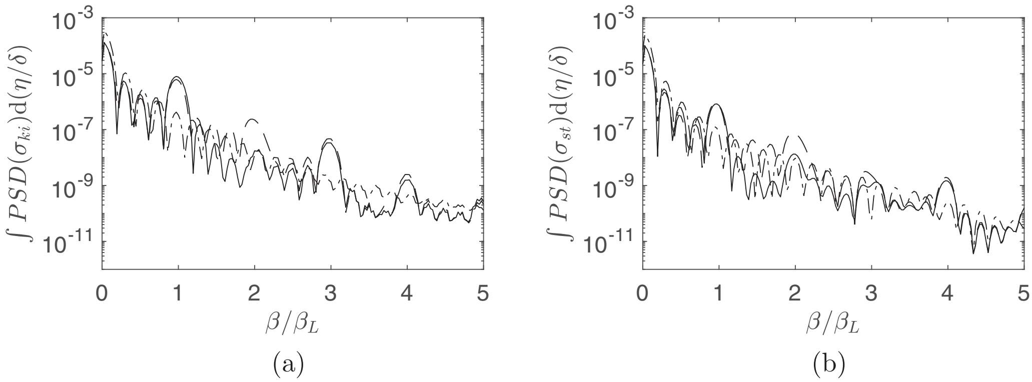

FIG. 16. Integrated components of the disturbance energy at $\Delta\xi = 0.05$ mm in the wave-number domain for cases No. 5, 7, and 9 (——aligned, - - - staggered, -·-·-single): (a) kinetic disturbance energy and (b) state disturbance energy.

to the total disturbance energy is higher than for σ_{st}. This is most evident at β_L and $3\beta_L$. Again, the main difference between the two distributed roughnesses occurs at $2\beta_L$.

To evaluate the development of the perturbation in the wake of the roughness, the PSD components at β_L and $2\beta_L$ are computed in subsequent $\eta-\zeta$ slices from $\Delta\xi = -0.95$ mm just $L/2$ upstream of the roughness up to $\Delta\xi = 1.2$ mm downstream of the roughness. For the "single" configuration, only the data in the wake starting from $\Delta\xi = 0.05$ mm is considered. The disturbance energy and its components are plotted in Fig. 17. The distributions in Figs. 17(a)–17(c) show that the development of disturbance energy at β_L can be split into four regions. First, there is growth up to the rear of the first row of elements at $\Delta\xi = -0.75$ mm. Then, to $\Delta\xi = 0.05$ mm, the levels remain almost constant implying saturation. In fact, the trend is rather decreasing implying even weaker disturbances downstream of the 100×100 roughness elements of the experiments in Ref. [24]. Third, both components of the disturbance energy decay severely and reach a local minimum. The minimum of the disturbance energy component related to the state of the fluid is located further upstream than for the component determined by the velocity perturbation. Therefore, the local minimum of the total disturbance energy in Fig. 17(c) is less distinct than the minima of its components and it is located between these minima. The growth downstream of the minima in Figs. 17(a)–17(c) is evident for all cases of distributed roughness. Wake disturbances induced by the "aligned" configuration of the corresponding experiments are more intense than for the "staggered" configuration.

The circles in Fig. 17(a) denote E_{ki} considering only the streamwise velocity perturbation $u'/(\overline{u}\sqrt{\overline{\rho}/\rho_e})$ for the "aligned" configuration. Whenever streaks at the fundamental wave number occur, i.e., upstream and downstream of the local minimum at $\Delta\xi \approx 0.4$ mm, it is sufficient to consider the streamwise velocity perturbation. However, the disturbance energy gain G is based on the lowest value of disturbance energy and cannot be computed using only the streamwise velocity perturbation. For the comparison of gains, consistent definitions of the kinetic disturbance energy are crucial. The circles in Fig. 17(b) denote a simplified computation of E_{st} using only the temperature perturbations $T'/(\overline{T}\sqrt{\gamma-1}\mathrm{Ma}_e)$ which will be motivated in Sec. IV C 4. The circles in Fig. 17(c) define the sum of the corresponding data from Figs. 17(a) and 17(b) and give a good approximation of the total disturbance energy.

The effect of the finite extent of the distributed roughness on the disturbance energy components and their gain at the fundamental wave number can be evaluated by comparing the distributed roughnesses to case "single" in Figs. 17(a) and 17(b). For both components, the disturbance energy of all the cases is of identical order at the location of the local minimum downstream of the roughness. Therefore, interference of disturbances induced by the elements with higher harmonics

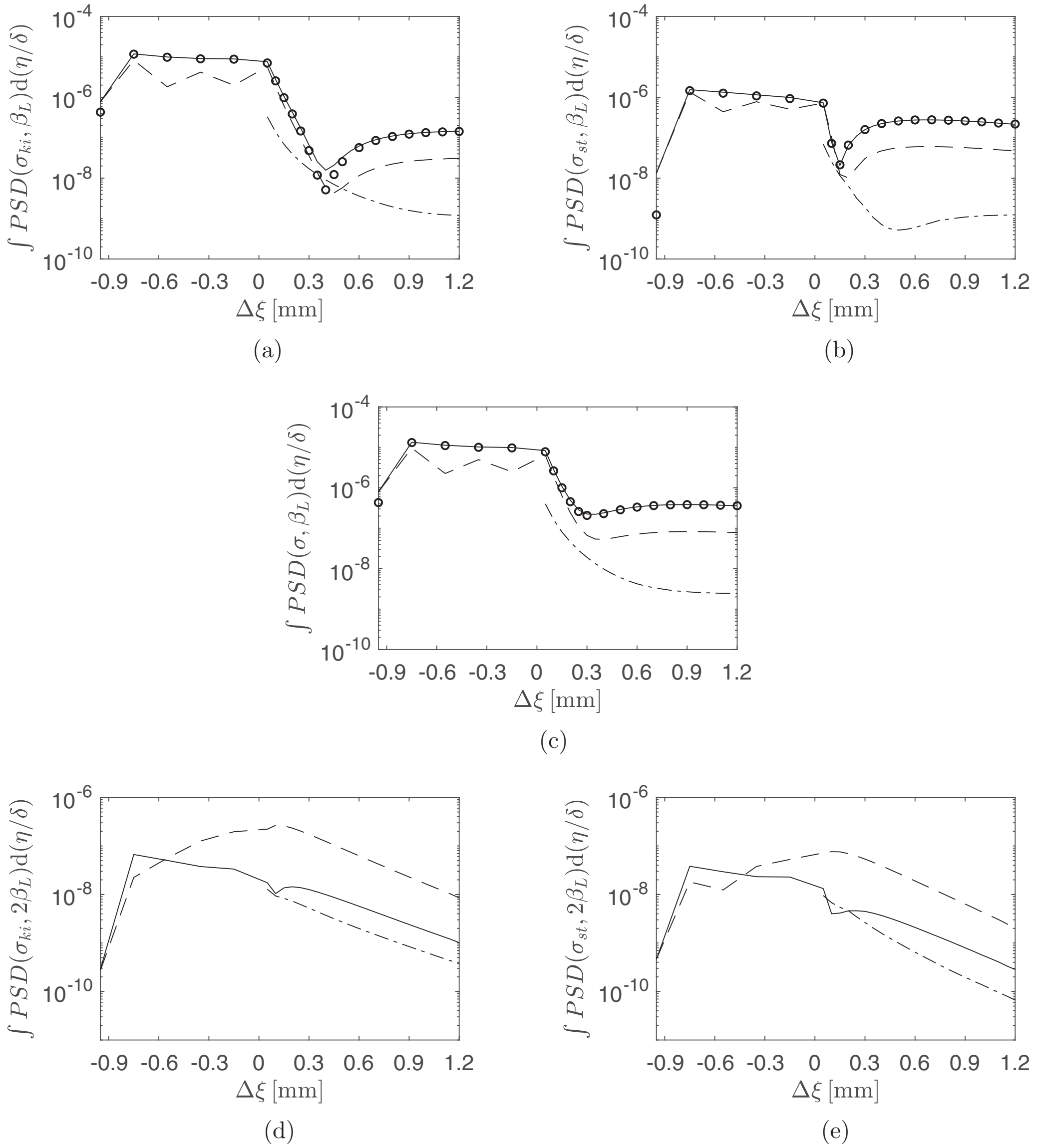

FIG. 17. Development of integrated PSDs of disturbance energy in η-ζ planes for cases No. 5, 7, and 9 (——aligned, - - - staggered, -·-·-single): (a) kinetic disturbance energy at the fundamental wave number β_L, the circles "○" denote PSD data of $u'/(\overline{u}\sqrt{\overline{\rho}/\rho_e})$ for case "aligned"; (b) state disturbance energy at β_L, the circles "○" denote PSD data of $T'/(\overline{T}\sqrt{\gamma-1}\mathrm{Ma}_e)$ for case "aligned"; (c) total disturbance energy at β_L, the circles "○" denote the sum of the circle data in (a) and (b); (d) kinetic disturbance energy at the second harmonic wave number $2\beta_L$; (e) state disturbance energy at $2\beta_L$.

of the disturbance field related to the overall extent of the roughness distribution is apparent. By defining the input disturbance E_{in}, the disturbance energy at the minimum downstream of the roughness introduces uncertainty into the gain G. The total disturbance energy in Fig. 17(c) is less affected by this interference. Between the locations of the minima of the disturbance energy components, i.e., at the minimum of the total disturbance energy, the decaying kinetic disturbance energy and the increasing disturbance energy related to the state of the fluid are more intense and

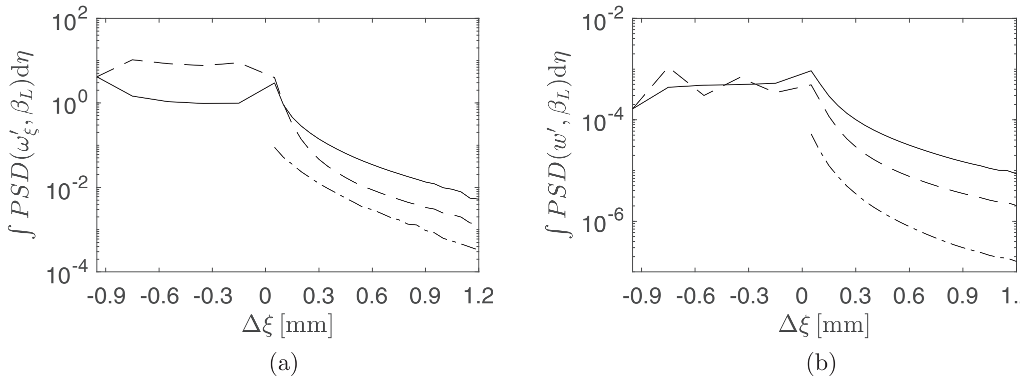

FIG. 18. Integrated PSDs of quantities driving the lift-up effect at β_L in η-ζ planes for cases No. 5, 7, and 9 (——aligned, - - - staggered, -·-·-single): (a) streamwise vorticity perturbation; (b) wall normal velocity perturbation.

less affected by the disturbance field determined by the overall extent of the distributed roughness. For the experimental "aligned" roughness layout, the disturbances of case "single" are one order of magnitude lower. That is, for comparison of the DNS results with potential experimental data or the optimal transient growth data in Sec. IV C 5, the gain of the total disturbance energy is considered.

The disturbance energy contained at $2\beta_L$ shows another growth behavior and additionally differs comparing the types of distributed roughness. Again, the analysis holds for the kinetic disturbance energy in Fig. 17(d) and the disturbance energy related to the state of the fluid in Fig. 17(e). As aforementioned in the analysis of the streamwise velocity perturbation in Fig. 15(d), the origin of the disturbance at the second harmonic varies and leads to higher amplitudes downstream of the roughness at $\Delta\xi = 0.05$ mm for the staggered configuration. Then, some small growth on a short streamwise interval can be observed. For $\Delta\xi \geqslant 0.3$ mm, the disturbance energy for all cases monotonically decays. Therefore, the following analysis of the growth mechanism focuses on the fundamental wave number.

4. Mechanism of transient growth

It is well known that the disturbance modulation in the wake of the elements is driven by streamwise vorticity inducing lift-up and down-wash in the perturbed laminar boundary layer. In Fig. 18, the PSDs of the streamwise vorticity and wall normal velocity component at β_L are shown. When the fluid undergoes rotation in the boundary layer, both quantities decrease monotonically downstream of the distributed roughness.

The disturbance fields are analyzed next. From the analysis of the disturbance energy at the fundamental wave number β_L, three locations are extracted. First, the final perturbation downstream of the roughness and preceding the severe decay is of interest. Likewise results were already presented in Fig. 15. Second, the later minimum initiating the disturbance growth is scrutinized. Since it is the minimum, this disturbance field has the highest gain of disturbance energy. Finally, the disturbance field subsequent to the growth is presented. The corresponding locations for the kinetic disturbance energy in Fig. 17(a) are considered.

The velocity disturbances occurring at the remaining two locations, i.e., of the minimum of disturbance energy and the subsequent maximum upstream of $\Delta\xi = 1.2$ mm, are shown in Fig. 19. The streamwise velocity in Figs. 15(a), 19(a), and 19(d) reflects the development of the kinetic disturbance energy. The vorticity turns the low-speed streaks downstream of the elements into high-speed streaks. The minimum of the disturbance energy occurs in the region where the wake is most homogeneous, i.e., the differences between the flow downstream of the roughness elements and in between are small. The velocity perturbations in the ζ-η plane show the vorticity decay

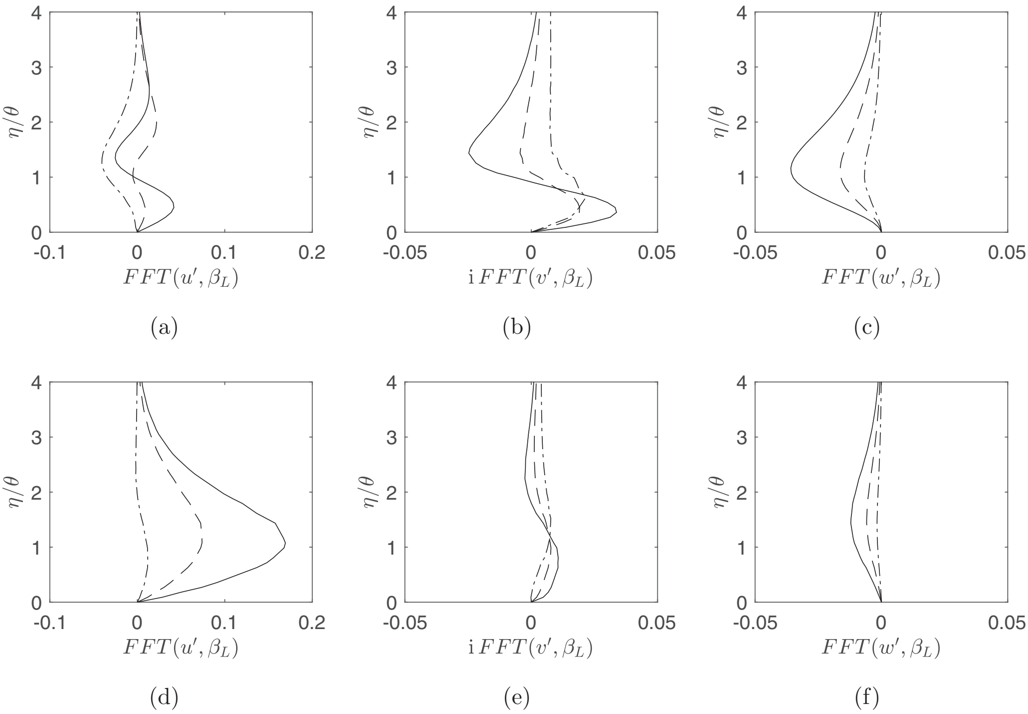

FIG. 19. Wall normal distribution of the velocity perturbation for cases No. 5, 7, and 9 (——aligned, - - - staggered, -·-·-single): (a)–(c) At the location of the minimum kinetic disturbance energy; for the configuration "single," the location of the aligned configuration is adopted; (d)–(f) at $\Delta\xi = 1.2$ mm, the end of the region with increased grid refinement.

at constant rotational direction. In other words, there is no change of sign in the wall normal velocity disturbance, hence the lift-up and down-wash remain at constant azimuthal position. The mechanism for both distributed roughnesses is identical, but leads to more intense streaks for the aligned configuration used in the experiments in Ref. [24].

Recalling the discussion of the gains G based on the disturbance energy in Sec. IV C 3, Fig. 19(a) illustrates the intensity of the distributed roughness cases and the "single" configuration at the location of the kinetic disturbance energy minimum to be similar.

The development of the disturbance energy component related to the state of the fluid in Fig. 17(b) is analyzed analogously. Figure 20 shows the wall normal temperature distributions at the fundamental wave number β_L. Since the wall normal temperature gradient in the unperturbed boundary layer is positive, the wall normal displacement of fluid induced by the streamwise vorticity leads to a temperature perturbation pattern similar to the velocity streaks. This is evident when Figs. 15(a) to 20(a), 19(a) to 20(b), and 19(d) to 20(c) are compared. Assuming negligible pressure perturbations in the boundary layer $p' = 0$, the linearized equation of state directly relates density and temperature perturbations via $T' = -\overline{T}\rho'/\overline{\rho}$. The circles in Fig. 20 denote this reconstruction of the temperature perturbation distribution from the density perturbation and the unperturbed boundary layer. At all three streamwise locations in Fig. 20, the reconstructed distributions agree well with the original data. Reconsidering the two terms in Eq. (6) for the state dependent disturbance energy, they can be combined using $p' = 0$ and $\overline{p} = p_{\mathrm{ref}}$ from boundary-layer theory. Then, the first term in Eq. (6) can be dropped and the last term reads $T'/(\overline{T}\sqrt{\gamma - 1}\mathrm{Ma}_{\mathrm{ref}})$. The circles in Fig. 17(b) show the reevaluation of the disturbance energy related to the state of the fluid applying this simplification. Except for the first location upstream of the distributed roughness, good

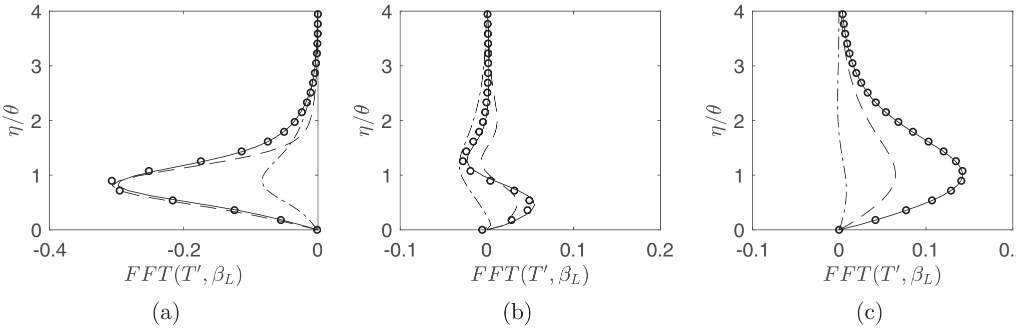

FIG. 20. Wall normal distribution of the temperature perturbation for cases No. 5, 7, and 9 (——aligned, - - - staggered, -·-·-single). The circles "∘" denote a reconstruction of the data based on the linearized equation of state and $p' = 0$, i.e., $T' = -\overline{T}\rho'/\overline{\rho}$, for case "aligned": (a) at $\Delta\xi = 0.05$ mm downstream of the distributed roughness; (b) at the location of the minimum disturbance energy related to the state of the fluid; for the "single" configuration, the location of the aligned configuration is adopted; (c) at $\Delta\xi = 0.65$ mm, the location of the local maximum of disturbance energy related to the state of the fluid.

agreement with the original data is obtained. Hence, also the gain G can be computed using only temperature or density perturbations. Similarly to the discussion of Fig. 15(a), the non-negligible temperature perturbation of case "single" in Fig. 20(b) indicates the uncertainty on the gain of the disturbance energy related to the state of the fluid.

To finalize the analysis of the roughness induced disturbances and their growth, the findings of the DNS are compared to results of optimal transient growth theory.

5. Comparison to optimal transient growth theory

Optimal transient growth theory computes the initial perturbation field undergoing the most intense growth that leads to the highest gain G. Here the optimization is defined by the fundamental azimuthal wave number β_L, the location of the roughness as starting point, and the objective function, i.e., the maximization of the total disturbance energy E at some position downstream of the roughness. For details regarding the governing equations and the adjoint-based optimization methodology, the reader is referred to Hein *et al.* [23]. The resulting velocity disturbance field for the present flow configuration is shown in Fig. 21. As expected, the optimal disturbance corresponds

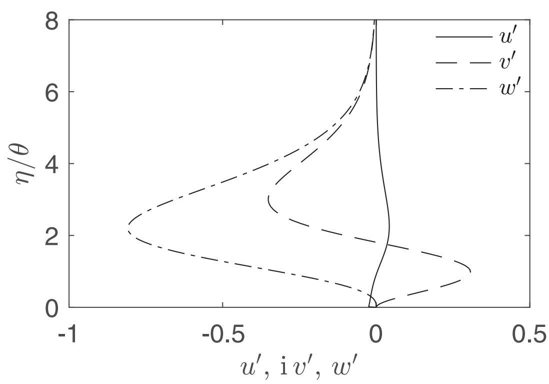

FIG. 21. Wall normal distribution of the velocity perturbation obtained applying optimal transient growth theory by Hein *et al.* [23] for the fundamental wave number β_L at the location of the roughness. The objective function of the optimization is to maximize the total disturbance energy E.

to a streamwise vortex with a rather weak streamwise velocity perturbation. The highest velocity occurs in the wall normal velocity component. This disturbance field is compared to the perturbation field in the DNS having the minimum kinetic disturbance energy in Figs. 19(a) to 19(c). Most notably, the optimal disturbance spans over the entire boundary layer up to $\delta/\theta = 7.79$, whereas the disturbance induced by the roughness extends only up to $\delta/\theta = 4$. The streamwise velocity perturbation in the DNS is found to be on the same order of magnitude as the velocity disturbances in the ζ-η plane. That is, although both distributed roughness configurations show gain by transient growth based on streamwise vortices, the disturbance differs tremendously in size and ratio of the velocity components from the optimal disturbance.

The total disturbance energy gain of the optimal disturbance in Fig. 21 at the fundamental wave number β_L is $G = 66.3$ on a length of 1.8 mm. The gain of the total disturbance energy in the DNS is $G = 1.74$ for the "aligned" configuration and $G = 1.553$ for the "staggered" case corroborating suboptimal growth. Amplification takes place over 0.55 mm and 0.5 mm.

At last, the findings of Sec. IV are discussed in the context of the state of the art considering the investigation of transition on re-entry capsules including the corresponding experiments in Ref. [24].

V. DISCUSSION

To identify the mechanism triggering boundary layer transition on the spherical forebody of an Apollo type re-entry capsule direct numerical simulations (DNS) of perturbed flow are analyzed. The perturbations consist of two deterministic configurations of micro-size distributed surface roughness that resemble subcritical surface imperfections in Ref. [26] and one configuration with a greater number of elements mounted on the capsule model of the corresponding experiments in Ref. [24]. The two roughnesses differ in the layout of the elements, i.e., aligned and staggered arrangements are considered. They are compared to analyze the sensitivity of the generated flow perturbations and to challenge the hypothesis that for vanishing differences between these alternate deterministic micro-size roughness configurations, stochastic roughnesses may be represented by deterministic roughnesses in numerical simulations or controlled experiments. The analysis is performed at two Reynolds numbers, i.e., $\mathrm{Re}_L = 1\,062\,500$ and $\mathrm{Re}_H = 3\,060\,000$.

The wakes of the distributed roughnesses at both Reynolds numbers possess common properties. The azimuthal disturbance distribution contains scales defined by the finite extent of the distribution and the geometric properties of the distribution. Since the distribution of the roughness elements in the experiments in Ref. [24] has a larger extent, the wake is decomposed applying a Fourier transformation to analyze the latter effect. To investigate the effect of the overall extent of the distributed roughness, analytic power-spectral densities and findings of a DNS configuration of a single roughness element covering the complete base area of the distributed surface imperfections are considered.

At the low Reynolds number where transitional flow is not observed in the experiments in Refs. [24,26], both types of distributed roughness induce almost identical disturbances on the boundary layer. In other words, at the lowest Reynolds number based on the roughness height Re_{kk} the disturbances are determined only by the final row of roughness elements and their azimuthal extent. The upstream character does not affect the receptivity process. At the high Reynolds number, transition occurs in the experiments in Ref. [24] under increased freestream noise conditions. For this configuration, the current results show distinct differences between the roughness patterns. That is, the receptivity process is also defined by the upstream distribution of the roughness elements. For the lower Reynolds number, the ratio of roughness height k and momentum thickness θ is $k/\theta = 0.295$. For the higher Reynolds number, it is $k/\theta = 0.529$. The transition correlation based on transient growth by Reshotko and Tumin [32] fits the transition data of Reda [36,37] starting at $k/\theta = 0.57$ [24]. The receptivity process of transition induced by transient growth depends on the roughness height and the azimuthal and streamwise distribution.

The differences between the two types of roughness arrays show clearly in the discussion of the fundamental wave number and its second harmonic. Disturbances at the fundamental wave number are more intense for the experimental configuration of aligned rows of elements. By analyzing the streamwise vorticity or wall normal velocity perturbation, their augmentation can be linked to transient growth due to the lift-up effect. At the second harmonic of the fundamental wave number, the staggered roughness arrangement leads to stronger disturbances. However, they can not be attributed to harmonics since they are explicitly generated at the staggered rows.

While the disturbance energy components at the fundamental wave number during the growth downstream of the distributed roughness are hardly affected by the smaller azimuthal extent of the DNS configuration in comparison to the setup of the corresponding experiments, the gain of the components is corrupted by uncertainties of the lowest value defining the input disturbance energy. When the sum of all components is considered for the computation of the gain, i.e., the total disturbance energy, the location of the input disturbance energy differs from the location of the minima of its components. Then, for the experimental "aligned" roughness layout, there is a difference of one order of magnitude between effects related to the roughness distribution and disturbances related to the overall extent of the distributed roughness at the fundamental wave number. In other words, a better ratio of signal, i.e., effects due to the distribution of elements, to noise, i.e., artificial effects due to the differing overall extent, is achieved and the comparability to experiments and optimal transient growth theory is enhanced. The smaller streamwise extent of the DNS compared to the experiments generates more intense disturbances.

The comparison of the most amplified disturbance at the fundamental wave number to results of optimal transient growth theory based on the total disturbance energy shows that streamwise vortices define the identical type of disturbance. However, the vortex computed in the DNS is restricted to the lower half of the boundary layer whereas the optimal disturbance extends up to the edge of the boundary layer. The disturbance gain and length of growth are suboptimal. Furthermore, the DNS also contain disturbances at other wave numbers. The most prominent additional perturbation occurs at wave number zero which alters the flow being displaced by the vortices and excites nonlinear effects.

Considering the aforementioned hypothesis, the present results lead to the following interpretation as to the identification of the transition mechanism in Refs. [24,26]. To identify the mechanism of boundary layer transition initiated by small disturbances that grow subsequently, the most amplified wave numbers from transitional data are to be compared to those of possible candidates, e.g., crossflow instabilities, first mode instabilities, or transient growth. If transition is initiated by stochastic distributed roughness and the relevant wave numbers of the transition process can not be identified because of, e.g., limited access to the measurement data or enormous computational cost, the transition scenario can be experimentally reproduced using deterministic distributed roughness matching and exciting the relevant wave numbers in the streamwise and azimuthal direction. Then, the identification of the relevant wave numbers of the stochastic distributed roughness can be achieved by investigating various configurations of deterministic distributed roughnesses in a parameter study. It goes without saying that this procedure could be very demanding due to the production time and cost of a single roughness configuration. To decrease the number of experiments, the wave-number distribution of the stochastic roughness can successively be divided among several deterministic roughnesses. The more wave numbers are contained in a single deterministic roughness, the closer it is to the stochastic roughness and the advantage of few wave numbers as candidates to identify the relevant transition mechanism is lost. However, successively decomposing the stochastic distributed roughness and excluding irrelevant wave numbers seems a promising approach to reduce time and cost.

In the current study, the disturbances in the DNS generated by the roughness are weak and do not exceed their initial amplitude during the short period of growth. In accordance with this finding, the experiments in Ref. [24] do not show any transitional data due to the low wind tunnel noise. In a follow-up study, the effect of freestream disturbances, more precisely freestream vorticity, leading to transitional flow in combination with the micro-sized roughness is analyzed to show how interactions alter the receptivity of the boundary layer and the disturbance growth.

ACKNOWLEDGMENTS

This work has been funded by the German Research Foundation (DFG) within the HYPTRANS PAK742. The support is gratefully acknowledged. Computing resources were provided by the High Performance Computing Center Stuttgart (HLRS) and the Jülich Supercomputing Center (JSC). The authors thank Alexander Theiss and Dr. Stefan Hein for providing the optimal transient growth results.

---

[1] M. M. S. Khan and E. Reshotko, Stability of the laminar boundary layer on a blunted plate in supersonic flow, in *Laminar-Turbulent Transition*, edited by R. Eppler and H. Fasel (Springer-Verlag, Berlin, 1980), pp. 186–200.

[2] P. A. Gnoffo, Planetary-entry gas dynamics, Annu. Rev. Fluid Mech. **31**, 459 (1999).

[3] J. D. Anderson Jr., *Hypersonic and High Temperature Gas Dynamics* (AIAA, Reston VA, 2000).

[4] S. P. Schneider, Summary of hypersonic boundary-layer transition experiments on blunt bodies with roughness, J. Spacecr. Rockets **6**, 1090 (2008).

[5] T. J. Horvath, S. A. Berry, and N. R. Merski, Hypersonic boundary/shear layer transition for blunt to slender configurations: A NASA langley experimental perspective, RTO-MP-AVT-111, 22 (2004).

[6] L. Lees, Laminar heat transfer over blunt-nosed bodies at hypersonic flight speeds, J. Jet Prop. **26**, 259 (1956).

[7] J. A. Fay and F. R. Riddell, Theory of stagnation point heat transfer in dissociated air, J. Aeronaut. Sci. **25**, 73 (1958).

[8] G. Strouhal, D. M. Curry, and J. M. Janney, Thermal protection system performance of the Apollo command module, AIAA Paper 1966-1718 (1966).

[9] J. J. Bertin, The effect of protuberances, cavities, and angle of attack on the wind-tunnel pressure and heat-transfer distribution for the Apollo command module, NASA TM X-1243 (1966).

[10] J. J. Bertin and R. M. Cummings, Critical hypersonic aerothermodynamic phenomena, Annu. Rev. Fluid Mech. **38**, 129 (2006).

[11] R. B. Erb, D. H. Greenshields, L. T. Chauvin, J. E. Pavlosky, and C. L. Statham, Apollo thermal-protection system development, J. Spacecr. Rockets **7**, 727 (1970).

[12] S. A. Berry, T. J. Horvath, R. P. Lillard, B. S. Kirk, and A. M. Cassady, Aerothermal testing for project Orion crew exploration vehicle, AIAA Paper 2009-3842 (2009).

[13] M. MacLean, E. Mundy, T. Wadhams, M. Holden, and R. Parker, Analysis and ground test of aerothermal effects on spherical capsule geometries, AIAA Paper 2008-4273 (2008).

[14] K. T. Berger, Aerothermodynamic testing of the crew exploration vehicle at Mach 6 and Mach 10, J. Spacecr. Rockets **46**, 758 (2009).

[15] B. R. Hollis, K. T. Berger, T. J. Horvath, J. J. Coblish, J. D. Norris, R. P. Lillard, and B. S. Kirk, Aeroheating testing and predictions for project Orion crew exploration vehicle, J. Spacecr. Rockets **46**, 766 (2009).

[16] L. M. Mack, Boundary-layer linear stability theory, AGARD Rep. No. 709 (1984).

[17] W. S. Saric, H. L. Reed, and E. B. White, Stability and transition of three-dimensional boundary layers, Annu. Rev. Fluid Mech. **35**, 413 (2003).

[18] M. V. Morkovin, Bypass transition to turbulence and research desiderata, in *Transition in Turbines*, edited by R. Graham, NASA Conf. Publ. 2386 (NASA, Washington, 1985), pp. 160–204.

[19] F. Li, M. Choudhari, C.-L. Chang, and J. White, Boundary layer transition over blunt hypersonic vehicles including effects of ablation-induced out-gassing, AIAA Paper 2011-3303 (2008).

[20] W. D. Henline, Y.-K. Chen, G. E. Palmer, and D. A. Stewart, Trajectory based, 3-dimensional heating and ablation calculations for the Apollo lunar/earth return capsule, AIAA Paper 1993-2788 (1993).

[21] H. L. Reed and W. S. Saric, Linear stability theory applied to boundary layers, Annu. Rev. Fluid Mech. **28**, 389 (1996).

[22] F. Li, M. Choudhari, C.-L. Chang, and J. White, Effects of injection on the instability of boundary layers over hypersonic configurations, Phys. Fluids **25**, 104107 (2013).
[23] S. Hein, A. Theiss, A. Di Giovanni, T. Schilden, W. Schröder, P. Paredes, M. M. Choudhari, F. Li, and E. Reshotko, Numerical investigation of roughness effects on transition on spherical capsules, J. Spacecr. Rockets **56**, 388 (2019).
[24] R. Radespiel, S. R. C. Ali, F. Muñoz, R. Bowersox, A. Leidy, H. Tanno, L. C. Kirk, and E. Reshotko, Experimental investigation of roughness effects on transition on blunt spherical capsule shapes, J. Spacecr. Rockets **56**, 405 (2019).
[25] A. Theiss, S. Hein, S. R. C. Ali, and R. Radespiel, Wake flow instability studies behind discrete roughness elements on a generic re-entry capsule, AIAA Paper 2016-4382 (2016).
[26] A. Theiss, S. Hein, D. Heitmann, S. R. C. Ali, and R. Radespiel, Numerical and experimental investigation of laminar-turbulent boundary layer transition on a blunt generic re-entry capsule, AIAA Paper 2014-2353 (2014).
[27] A. Theiss and S. Hein, Investigation on the wake flow instability behind isolated roughness elements on the forebody of a blunt generic re-entry capsule, in *Progress in Flight Physics*, Vol. 9 (EDP Sciences, Les Ulis, France, 2017), pp. 451–480.
[28] P. J. Schmid and D. S. Henningson, *Stability and Transition in Shear Flows* (Springer-Verlag, New York, 2001).
[29] J. J. Buglia, Heat transfer and boundary-layer transition on a highly polished hemisphere-cone in free flight at Mach numbers up to 3.14 and Reynolds numbers up to 24×10^6, NASA TN D-955 (1961).
[30] E. Reshotko and A. Tumin, The blunt body paradox—A case for transient growth, in *Laminar-Turbulent Transition*, edited by H. Fasel and W. Saric (Springer-Verlag, Berlin, 2000), pp. 403–408.
[31] E. Reshotko, Transient growth: A factor in bypass transition, Phys. Fluids **13**, 1067 (2001).
[32] E. Reshotko and A. Tumin, Role of transient growth in roughness-induced transition, AIAA J. **42**, 766 (2004).
[33] E. Reshotko, Transition issues for atmosheric entry, J. Spacecr. Rockets **45**, 161 (2008).
[34] P. Paredes, M. M. Choudhari, and F. Li, Blunt-body paradox and transient growth on a hypersonic spherical forebody, Phys. Rev. Fluids **2**, 053903 (2017).
[35] M. T. Landahl, A note on an algebraic instability of inviscid parallel shear flow, J. Fluid Mech. **98**, 243 (1980).
[36] D. C. Reda, Correlation of nosetip boundary-layer transition data measured in ballistics-range experiments, AIAA J. **19**, 329 (1981).
[37] D. C. Reda, Review and synthesis of roughness-dominated transition correlations for reentry applications, J. Spacecr. Rockets **39**, 161 (2002).
[38] R. G. Batt and H. H. Legner, A review of roughness-induced nosetip transition, AIAA J. **21**, 7 (1983).
[39] A. N. Leidy, E. Reshotko, F. Siddiqui, and R. D. W. Bowersox, Transition due to roughness on blunt capsule: Comparison with transient growth correlation, J. Spacecr. Rockets **55**, 167 (2018).
[40] A. Demetriades, Roughness effects on boundary-layer transition in a nozzle throat, AIAA J. **19**, 282 (1981).
[41] T. Schilden, W. Schröder, S. R. C. Ali, J. Wu, A.-M. Schreyer, and R. Radespiel, Analysis of acoustic and entropy disturbances in a hypersonic wind tunnel, Phys. Fluids **28**, 056104 (2016).
[42] E. C. Marineau, D. R. Lewis, M. S. Smith, J. F. Lafferty, M. E. White, and A. J. Amar, Investigation of hypersonic laminar heating augmentation in the stagnation region, AIAA Paper 2013-0308 (2013).
[43] L. Schneiders, C. Günther, M. Meinke, and W. Schröder, An efficient conservative cut-cell method for rigid bodies interacting with viscous compressible flows, J. Comput. Phys. **311**, 62 (2016).
[44] A. Lintermann, S. Schlimpert, J. H. Grimmen, C. Günther, M. Meinke, and W. Schröder, Massively parallel grid generation on hpc systems, Comp. Methods Appl. Mech. Eng. **277**, 131 (2014).
[45] D. Hartmann, M. Meinke, and W. Schröder, An adaptive multilevel multigrid formulation for cartesian hierarchical grid methods, Comput. Fluids **37**, 1103 (2008).

[46] L. Schneiders, D. Hartmann, M. Meinke, and W. Schröder, An accurate moving boundary formulation in cut-cell methods, J. Comput. Phys. **235**, 786 (2013).

[47] A. Hanifi, P. J. Schmid, and D. S. Henningson, Transient growth in compressible boundary layer flow, Phys. Fluids **8**, 826 (1996).

[48] S. Zuccher, A. Tumin, and E. Reshotko, Parabolic approach to optimal perturbations in compressible boundary layers, J. Fluid Mech. **556**, 189 (2006).